PNNL-25319

Prepared for the U.S. Department of Energy
under Contract DE-AC05-76RL01830

Performance of Virtual Current Meters in Hydroelectric Turbine Intakes

SF Harding
PDJ Romero-Gomez
MC Richmond

Hydrology Group
Pacific Northwest National Laboratory
Richland, WA 99352

April 2016

Pacific Northwest NATIONAL LABORATORY
Proudly Operated by Battelle Since 1965

PACIFIC NORTHWEST NATIONAL LABORATORY
operated by
BATTELLE
for the
UNITED STATES DEPARTMENT OF ENERGY
under Contract DE-AC05-76RLO1830

Printed in the United States of America

Available to DOE and DOE contractors from the
Office of Scientific and Technical Information,
P.O. Box 62, Oak Ridge, TN 37831-0062;
ph: (865) 576-8401
fax: (865) 576-5728
email: reports@adonis.osti.gov

Available to the public from the National Technical Information Service,
U.S. Department of Commerce, 5285 Port Royal Rd., Springfield, VA 22161
ph: (800) 553-6847
fax: (703) 605-6900
email: orders@ntis.fedworld.gov
online ordering: http://www.ntis.gov/ordering.htm

This document was printed on recycled paper.
(9/2003)

PNNL-25319

Performance of Virtual Current Meters in Hydroelectric Turbine Intakes

SF Harding
PDJ Romero-Gomez
MC Richmond

Hydrology Group
Pacific Northwest National Laboratory
Richland, WA 99352

Summary

Standards provide recommendations for the best practices in the installation of current meters for measuring fluid flow in closed conduits. These include PTC-18 and IEC-41 . Both of these standards refer to the requirements of the ISO Standard 3354 for cases where the velocity distribution is assumed to be regular and the flow steady. Due to the nature of the short converging intakes of Kaplan hydroturbines, these assumptions may be invalid if current meters are intended to be used to characterize turbine flows. In this study, we examine a combination of measurement guidelines from both ISO standards by means of virtual current meters (VCM) set up over a simulated hydroturbine flow field.

To this purpose, a computational fluid dynamics (CFD) model was developed to model the velocity field of a short converging intake of the Ice Harbor Dam on the Snake River, in the State of Washington. The detailed geometry and resulting wake of the submersible traveling screen (STS) at the first gate slot was of particular interest in the development of the CFD model using a detached eddy simulation (DES) turbulence solution.

An array of virtual point velocity measurements were extracted from the resulting velocity field to simulate VCM at two virtual measurement (VM) locations at different distances downstream of the STS. The discharge through each bay was calculated from the VM using the graphical integration solution to the velocity-area method. This method of representing practical velocimetry techniques in a numerical flow field has been successfully used in a range of marine and conventional hydropower applications.

A sensitivity analysis was performed to observe the effect of the VCM array resolution on the discharge error. The downstream VM section required 11–33% less VCM in the array than the upstream VM location to achieve a given discharge error. In general, more instruments were required to quantify the discharge at high levels of accuracy when the STS was introduced because of the increased spatial variability of the flow velocity.

Acknowledgments

This research was funded by the U.S. Department of Energy, Energy Efficiency and Renewable Energy, Wind and Water Power Program.

Pacific Northwest National Laboratory (PNNL) is operated for the U.S. Department of Energy by Battelle Memorial Institute under Contract No. DE-AC06-76RLO 1830.

Computations described here were performed using the facilities of the PNNL Institutional Computing Center.

We also thank Susan Ennor and Cindy Rakowski for their help in preparing the report.

Abbreviations and Acronyms

ABBREV	DEFINITION
CFD	computational fluid dynamics
cfs	cubic feet per second
cm	centimeter(s)
DES	detached eddy simulation
DNS	direct numerical simulation
ERDC	Engineer Research and Development Center
ISO	International Standards Organization
kcfs	thousand cubic feet per second
km	kilometer(s)
LDV	laser Doppler velocimeter
LES	large eddy simulation
m	meter(s)
m^3/s	cubic meter(s) per second
ms	millisecond(s)
MW	megawatt(s)
MAE	mean absolute error
PNNL	Pacific Northwest National Laboratory
RANS	Reynolds-averaged Navier-Stokes
RMS	root-mean square
RPM	revolutions per minute
STS	submersible traveling screen(s)
TKE	turbulent kinetic energy
URANS	unsteady Reynolds-averaged Navier-Stokes
USACE	U.S. Army Corps of Engineers
VBS	vertical barrier screen(s)
VCM	virtual current meter(s)
VM	virtual measurement(s)

Contents

Figures

Tables

1.0 Introduction

Computational fluid dynamics (CFD) has been used to accurately model the flow field dynamics of hydroelectric turbine intakes (Khan et al. 2004a). In addition to the applications of power generation and hydrodynamic loading, such simulations can be used to quantify the biological effects of hydroturbines during fish passage. This report describes the development of such a model for the Ice Harbor Dam in Washington State, USA. The CFD model is then used to investigate the use of current meters for calculating the discharge through the intake for a variety of operating conditions.

Conventionally, the use of steady-state Reynolds-averaged Navier-Stokes (RANS) formulations is the industry practice for calculating engineering flows in domains of large extents, as in the turbine intake at Ice Harbor Dam. In RANS solutions, flow quantities associated with turbulent fluctuations—such as the turbulent kinetic energy and its rate of dissipation—are *modeled* by following empirical-analytical conservation equations. To explicitly *resolve* the velocity fluctuations, we must resort to turbulence modeling approaches that have proven accurate for canonical flows of simple configurations. We undertook the challenge of applying one such eddy-resolving technique—the detached eddy simulation (DES)—to compute the intake flows that feed into the evaluations of the performance of virtual current meters (VCM).

The RANS applications pertaining to hydropower flows are prevalent in both academia and industry. Steady-state RANS formulations have been used for evaluating fish passage conditions (Khan et al. 2004a,b), characterizing wicket gate-runner interactions (Nennemann et al. 2005), designing runner replacements (Prasad 2012, Roh et al. 2010), and proposing draft tube rehabilitation (Hellström et al. 2007). This has given rise intensive use of CFD tools for integral optimization of hydropower systems (Maruzewski et al. 2010, Wu et al. 2007). The DES applications in hydroturbines are, on the other hand, scarce. To the best of our knowledge, only a few studies have run runner and draft tube flows with DES. Normally, the criteria to select the DES strategy include targeting a highly dynamic flow condition and applying DES at physical scale models rather than prototype domains. Because the present application includes a submergible traveling guide structure that largely disturbs the flow and creates high turbulence, we used the computational capabilities at Pacific Northwest National Laboratory (PNNL) to achieve high turbulence flow resolution that can be used for the subsequent VCM analysis.

One industry standard of velocity measurement is the use of propeller-type current meters, which measure the velocity at a point as a function of the propeller rotational velocity. By deploying an array of current meters across the entire cross section of each bay, the velocity profile can be measured across the area. The discharge is then calculated by performing a double integral of the velocity profiles across the horizontal and vertical directions, known as the velocity-area method (ISO 2008a).

In this report, the velocity-area method of discharge calculation is performed by extracting point velocities from a time-averaged CFD velocity field to represent VCM measurements in the intake bays. This method of representing practical velocimetry techniques in a numerical flow field has been successfully used in a range of marine and conventional hydropower applications (Christian et al. 2015, Lee et al. 2015, Richmond et al. 2015, Harding et al. 2016).

The flow environment in question is highly heterogeneous due to the presence of submersible traveling screens (STS) that introduce steep velocity shears in their wake flows, which adversely affect the accuracy of the discharge calculation. The recovery of the flow disturbance through turbulent mixing reduces this effect with distance downstream of the STS. The effect of the STS installation on the accuracy of the virtual discharge measurement is investigated at two virtual measurement (VM) sections.

The specific objectives of this study are as follows:

- to accurately model the velocity field in a short converging intake in the vicinity of the STS using CFD.

- to calculate the total discharge through the intake using an array of VCM to extract point velocity data at two different VM sections. This is to be performed using the CFD solutions both with and without the STS present.

- to perform a sensitivity analysis of calculated discharge error in response to:
    - the array resolution of VCM.
    - the location of the VM section.

2.0 Site description

2.1 Ice Harbor Dam

The Ice Harbor project is owned and operated by the U.S. Army Corps of Engineers (USACE) Walla Walla District, and is located in Eastern Washington State on the Snake River at km 15.6 (Figure 2.1). The average annual river flow at the dam is approximately 1383 m^3/s (48,840 cfs). The dam consists of a concrete powerhouse, navigation lock, two fish ladders, a removable spillway weir, and a juvenile fish bypass facility. Construction of the Ice Harbor Dam began in 1956, and three generators were put in operation in 1961. Three more turbine units were installed and began to produce power in 1976. The powerhouse has an overall length of 205 m, and the 10-bay spillway is 180 m long and includes ten 15.24 m tainter gates. An aerial view is shown in Figure 2.2.

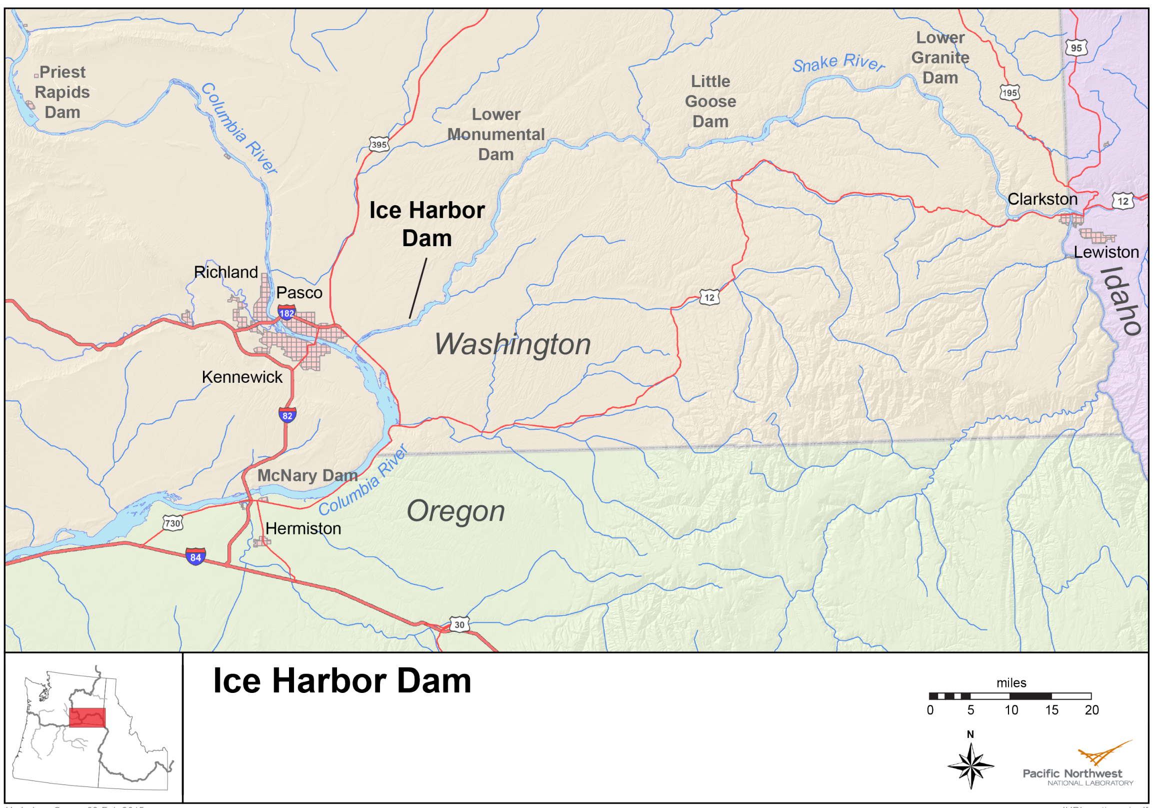

Figure 2.1. Location of the Ice Harbor Dam on the Snake River in Eastern Washington.

2.2 Intake and Turbine Unit

Although the present intake models do not include the hydroturbine unit (e.g., blades and draft tube), we consider it relevant to provide the context in which these modeling efforts take place. In addition to supporting studies of VCM, these simulations are used to quantify the biological performance of the hydroturbines during fish passage. Thus, the features of the turbine units in

Figure 2.2. Ice Harbor on the Snake River, Washington. The spillway is on the left, the powerhouse is on the right.

the powerhouse become critical. The powerhouse has six Kaplan turbine units. All units are 6-blade; Units 1 through 3 have a diameters of 7.11 m rotating at 90 RPM with rated power of 90 MW, while Units 4 through 6 have diameters of 7.62 m rotating at 87.5 RPM with rated power of 111 MW. This gives a total plant rated capacity of 603 MW.

The USACE intends to award a contract for design and delivery of a new turbine design to be installed in Unit 2. The description of the flows through Unit 2 was necessary to support quantitative studies of safer fish passage of the proposed units, compared to the current unit. The assessment of both the hydraulic and biological performances of the designs is included with CFD simulations that include the runner and supporting structures, e.g., the wicket gates, the stay vanes, the intake, the draft tube, etc.

Units 1 through 3 have the same geometry; they consist of 20 wicket gates with a maximum opening of 53.5° but rarely exceeding 47°, and 19 stay vanes (Figure 2.3). Another relevant feature of the intake model is the presence of the trash racks, which must be taken into consideration in the turbine runner design process. The present simulations incorporate the trash racks, and the flows of two intake geometries—with and without STS—are examined.

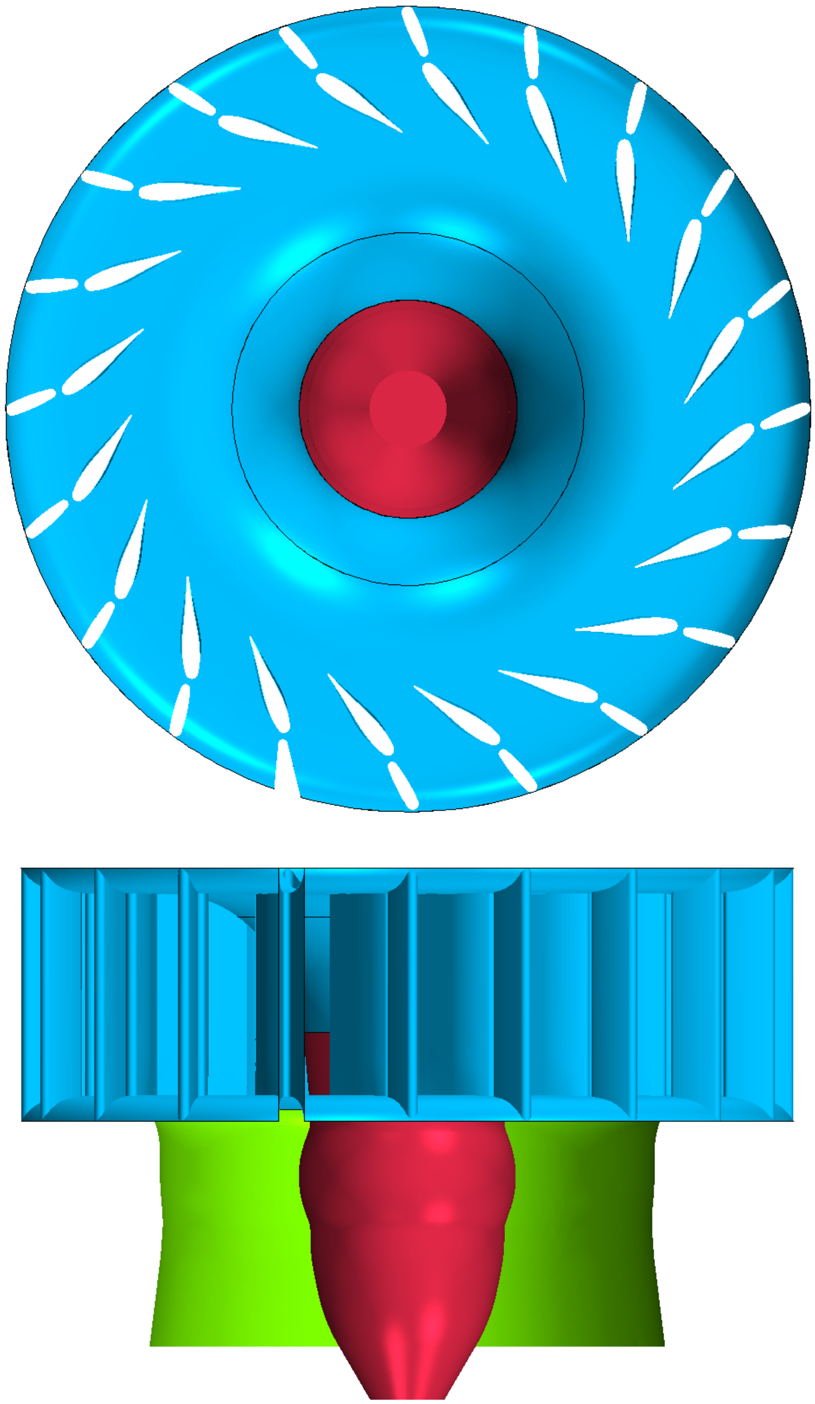

Figure 2.3. Top (upper) and side (lower) views of Unit 2 stay vanes and wicket gates in blue, hub in red, and discharge ring in green.

2.3 Submersible Traveling Screen

Submersible travel screens are deployed in each unit of the Ice Harbor Dam during nine months of the year. The STS are designed to route the juvenile salmonids away from the operating turbines and towards safer passage during the migration period. The STS guide fish into the gate slots. Within the upper portion of the unit (Figure 2.4), vertical barrier screens (VBS) are also deployed to further guide juvenile fish into orifices, then into a collection channel, which ultimately bypasses them around the dam. This turbine bypass aims to prevent the juvenile fish from crossing the hazardous flow conditions arising from the operation of the hydroturbine. The efficiency losses associated with the deployment of STS is 1 to 3% in comparison to the absence of STS; this loss is partly related to the flow disruption and large variability of the flow field in the vertical direction. The present work compares the flows arising from the two scenarios—with and without STS—in a quantitative manner.

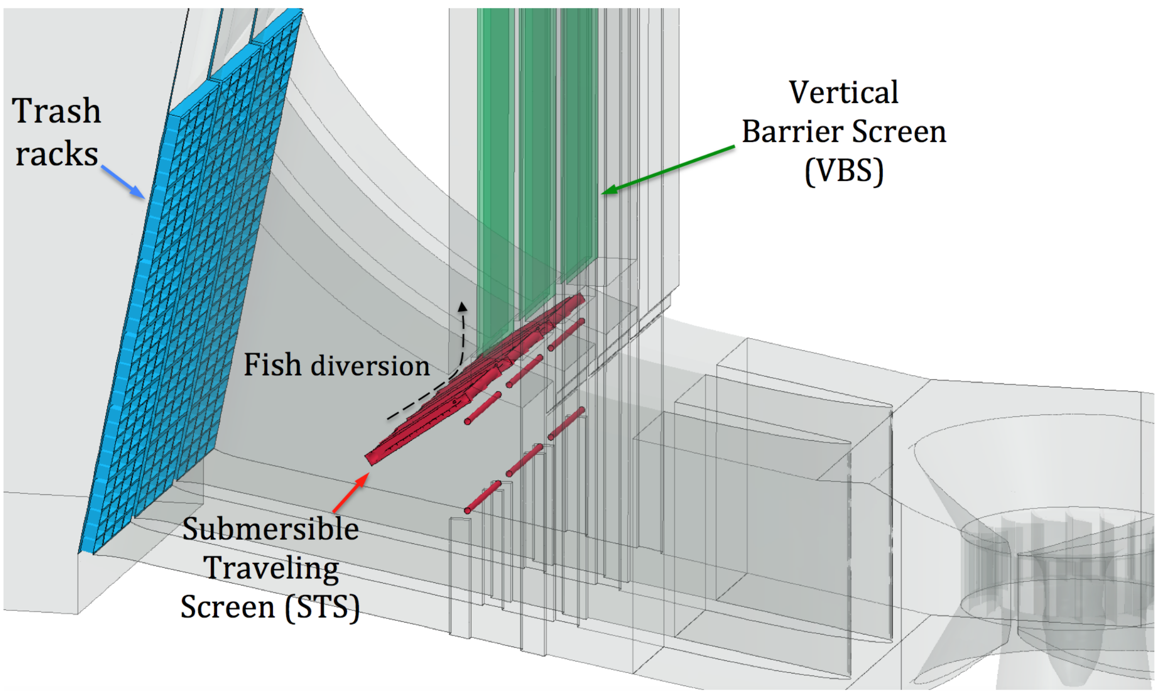

Figure 2.4. Trash racks (blue), submersible traveling screens (red), and vertical barrier screens (green) in the intake model.

3.0 Flow Simulation with Computational Fluid Dynamics

3.1 General Features of the CFD Model

The flow field within the intake was simulated with CFD simulations in combination with advanced turbulence modeling. The model geometry included the trash racks, gate slots, distributor, wicket gates, and stay vanes. A few modifications of the actual geometry were made to more efficiently produce CFD results appropriate for the present application. First, because a single unit was simulated, the domain upstream from the trash racks was extended with sides set as symmetry planes. In reality, some lateral flow occurs upstream from the trash racks. Second, because the representation of the runner blades in the original CFD model requires a large portion of the mesh cells, the runner was absent in the solutions presented in this document. Near the runner, the mesh density is high because flows are expected to have large gradients, and the correct quantification of moments and forces on the blade surfaces strongly depends on the local mesh resolution. However, it will be shown that the absence of the runner did not have any effect on the flow field upstream from the wicket gates and stay vanes. Third, the original model includes the draft tube, whereas the modified version included a continuous pipe extended below the discharge ring shown in Figure 2.3.

Two scenarios of the unit operation were simulated: with and without the STS. The deployed STS is indeed the most prevalent configuration in terms of proportion of the year (75%) during which it is deployed; for three months of the year the STS are retrieved because no downstream juvenile fish migration is expected then. The difference in geometry between the two configurations is shown in Figure 3.1. After the STS parts (shown in red on the left side of Figure 3.1) were removed, the gate slots were extended up to the top of the model. Other than these mentioned differences in geometry, the two models were essentially the same.

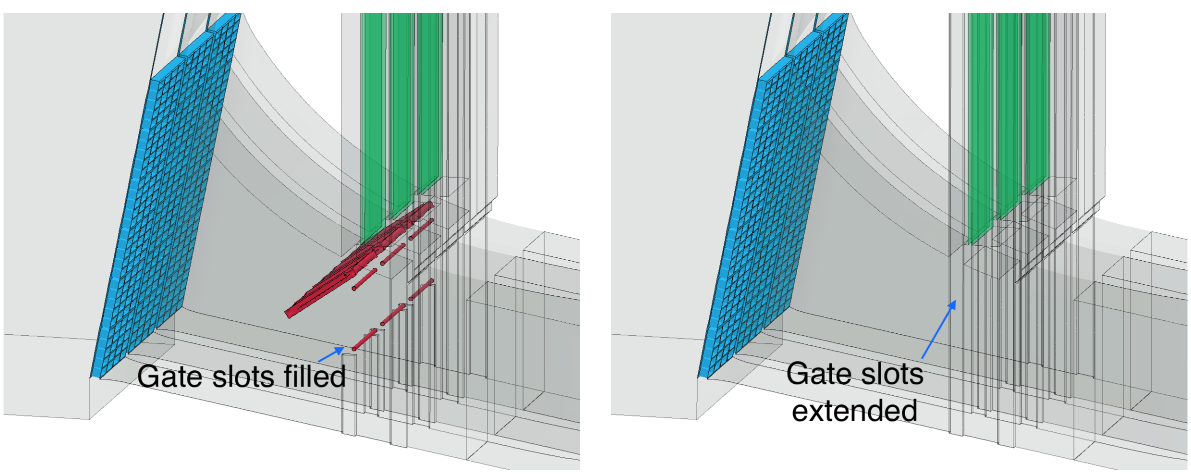

Figure 3.1. The intake model geometry, with (left) and without (right) the STS deployed.

The meshing and flow field calculation were done using the commercial software STAR-CCM+ v9 (CD-adapco 2014). A segregated flow solver with the Hybrid second-order Upwind/Central convection scheme was used with the DES approach (Section 3.2). The time discretization was second-order accurate, with the time solution advancing at 20-ms intervals ($\Delta t = 0.02s$). The selected time step ensured that the numerical solution remains within a Courant number less than unity, given an average velocity magnitude of $U = 2$ m/s, and a core mesh size (Δx) of 0.05 m, i.e., $U \cdot \Delta t/\Delta x < 1.0$. The inlet boundary was a uniform mass inflow to match the selected discharge. The incoming turbulence intensity was 1%, with a viscosity ratio (turbulent viscosity divided by fluid viscosity) set at 10. The pipe end was set as an outlet boundary. The STS was represented as three porous interfaces to account for the three resistances present: two meshed screens and one perforated plate, as shown in Figure 3.2. Likewise, the VBS (shown in green in Figure 2.3) was also modeled as a porous baffle with porosity and inertial resistance. The "No STS" scenario lacked all of the porous interfaces associated with the STS, and direct contact (no porous resistance) was modeled in the VBS. The remaining model boundaries were set as no-slip walls.

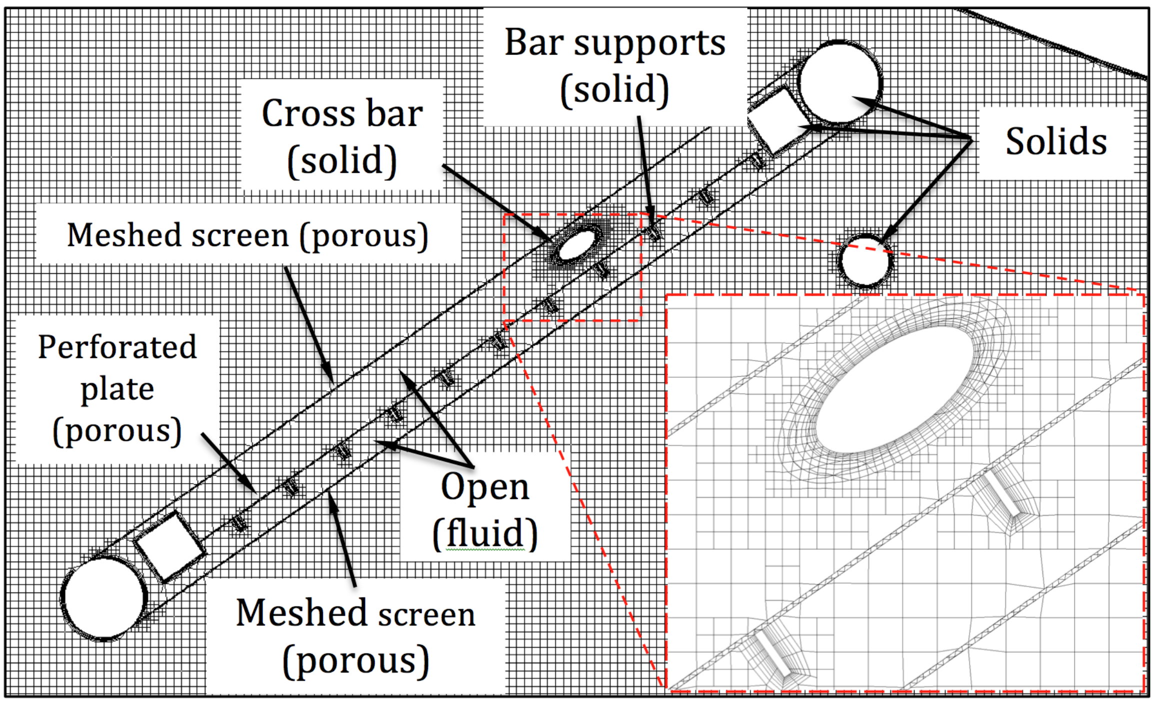

Figure 3.2. The STS consists of an assembly of flow-resistance materials (screens and perforated plates) mounted on solid structures. The mesh is shown in actual size, the core size (Δx) was equal to 5 cm.

The computational mesh was primarily composed of hexahedral cells of varying size. The volume upstream from the trash racks was coarse because nearly uniform incoming velocities were expected. The core cell size was 5 cm over the intake contraction spanning from the trash racks to the distributor, a portion that included the STS. The cell size was 10 cm elsewhere. The trash racks, stay vanes, and wicket gates represented geometric changes that required higher resolution on the surface (mesh shown in Figure 3.3). The wall y^+ was approximately 20 and 50 on the trash racks and wicket gates/stay vanes, respectively. Because of the differences between models with and without the STS, the mesh sizes were 128.2 M and 122.7 M, respectively.

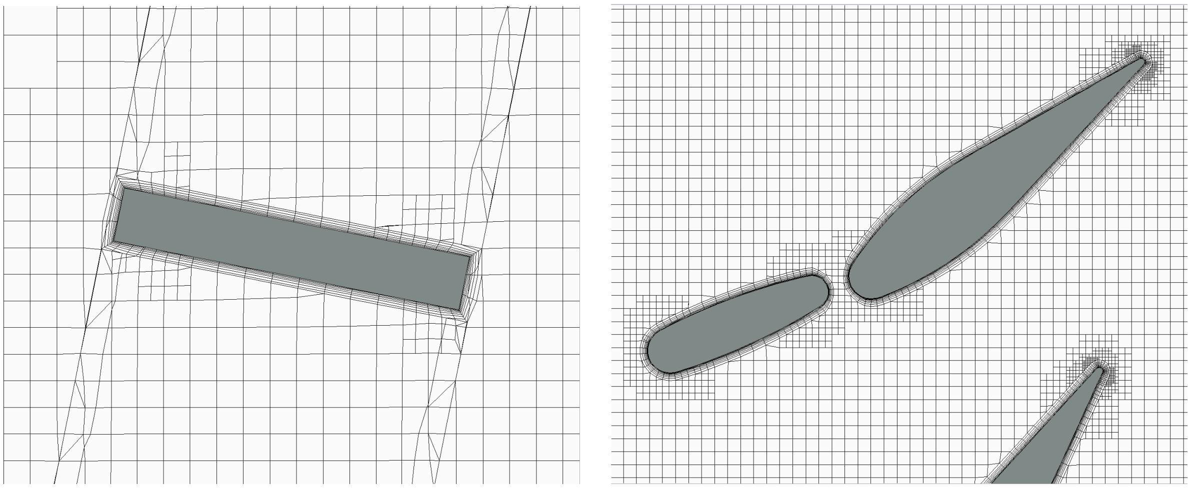

Figure 3.3. The mesh features finer cells near the trash racks (left) and the stay vanes/wicket gates regions (right).

Figure 3.4 shows the general features of both the mesh screens and perforated plate of the STS. These components are represented as porous interfaces arranged as shown in Figure 3.2. The pressure loss (ΔP) through the interface is modeled with porosity (ϕ) and inertial coefficients (α in Equation 3.1). Because of the high expected velocities through the baffles, the viscous resistance coefficient (β) was assumed to be zero. This reduced the formulation to a conventional hydraulic headloss equation (Equation 3.2) in which the parameter K can be known from empirical relationships specific to meshed screens and perforated plates. To determine K, we followed the guidelines for headloss associated with structures used in fish diversion projects (USBR 2006). Thus, the screen and the perforated plate had porosity values (ϕ) of 58% and 45%, respectively, and resistance coefficients α of 0.45 and 1.78 (dimensionless), respectively. For the vertical barrier screens, we followed the guidelines provided by the USACE Portland office in their dam operations, and selected values of $\phi = 27\%$ and $\alpha = 15.00$.

$$\Delta P = -\rho(\alpha|V_n| + \beta) \cdot V_n \tag{3.1}$$

$$\Delta h = K \cdot \frac{V_n^2}{2g} \tag{3.2}$$

We simulated a discharge of 386.9 m^3/s (13.66 kcfs), which was one of the discharges selected for testing hydraulic performance of the unit at the Engineering Research and Development Center (ERDC), a USACE facility in Vicksburg, Mississippi. This and other discharge conditions were selected as part of the design process of the new turbine runner in Unit 2. The laboratory runs were conducted at ERDC using a 1:25 scale physical hydraulic model of the turbine, intake

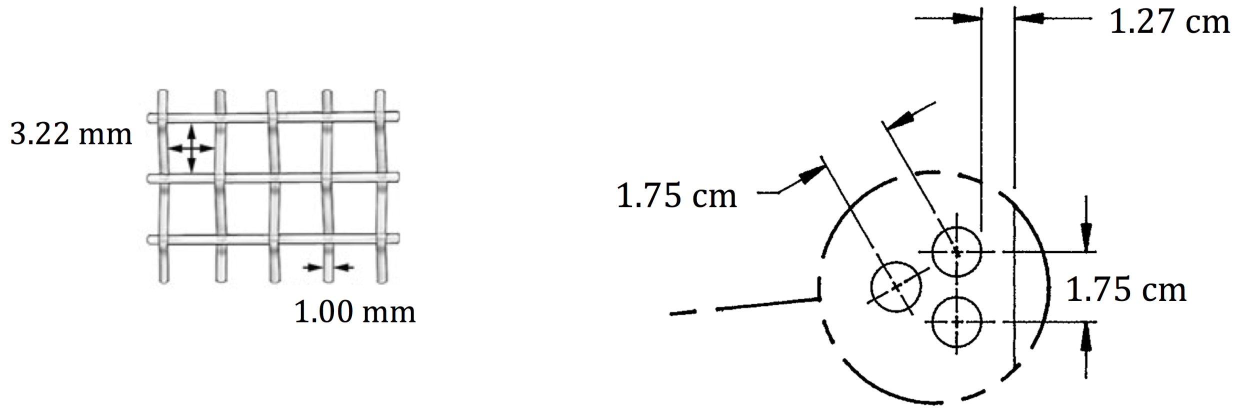

Figure 3.4. The STS consists of two meshed screens (left) and one perforated plate (right), the properties of which are modeled as porosity and inertial resistance coefficients in the CFD simulations.

and draft tube. During the laboratory runs, laser Doppler velocimeter (LDV) measurements were collected at three transects, hereinafter referred as the upstream, middle, and downstream transects (Figure 3.5). For the "STS model," mean and RMS velocities were made available for the stream-wise and vertical directions, or *U* and *W* velocities, respectively. These values will be used to validate the quality of the present CFD simulations with the STS in place. For the "No STS" version of the model, for which no LDV data were available, we then assumed that the numerical solution was of similar quality to the"STS" version because the meshing and solver settings remained the same in both versions.

Considering an estimated flow-through time between the STS and the runner zone, the simulation was "warmed up" over 5 times (60 s), and averaged over 3 times (30 s) thereafter. This, and the examination of velocity time series at various points within the domain, ensured that the time averages were taken when the solution was in statistical steady state. The simulation of each scenario took approximately 13 days to complete on 448 processors.

3.2 Turbulence Modeling with Detached Eddy Simulation

Complex flow fields surrounding civil infrastructure exhibit conditions that are highly variable in time and space and at different scales. An *ideal* flow simulation could describe such variations to the fullest extent; i.e., all variation scales would be explicitly *resolved* and output from a direct numerical simulation (DNS). Nevertheless, even the most powerful supercomputers to date are limited to simulate such full turbulent features only in simple canonical flows at low Reynolds numbers. Instead, to account for the effects of turbulence, all engineering applications must rely on various turbulence modeling approaches. The most common strategy in flows around large-scale engineering systems consists of *modeling* the turbulent fluctuations by averaging all scales, giving rise to the so-called RANS formulations. Between full resolution (DNS) and full modeling (RANS) of turbulent fluctuations, there exist approaches that selectively combine both turbulence modeling and resolution. The DES technique uses a RANS formulation near solid

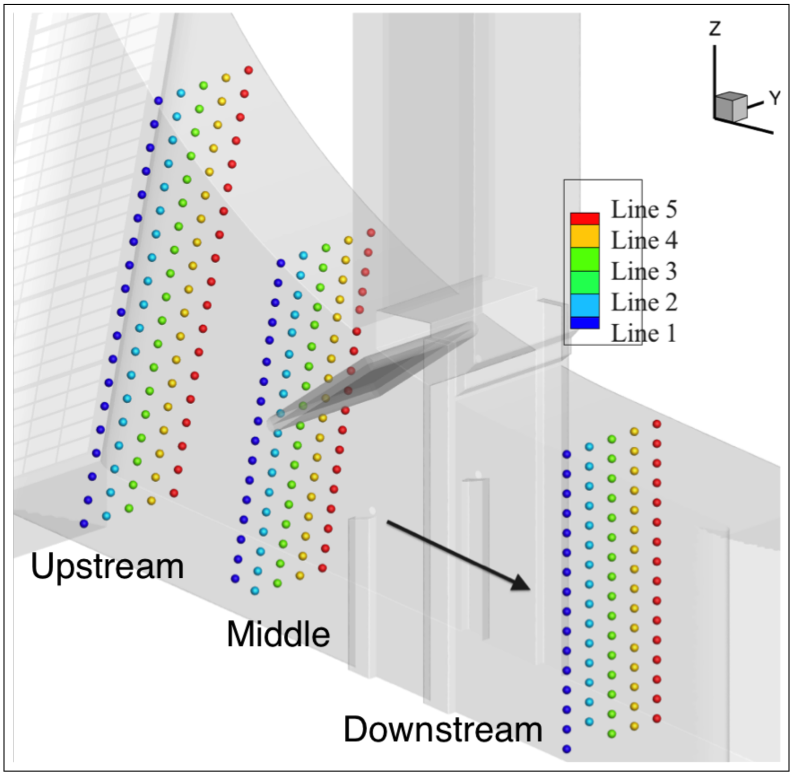

Figure 3.5. LDV data were collected at the points grouped in three transects: upstream, middle, and downstream

boundaries when the turbulent length scale is less than the cell size; otherwise, it assigns a large eddy simulation (LES) to explicitly resolve the flow field. In reality, with a DES, some portion of the turbulent fluctuations will be *resolved* and the remaining portion will be *modeled*. One of the objectives of the present study was to achieve the greatest turbulence resolution possible in the intake flow.

We used the DES version of the widely used SST k-ω model (Menter and Kuntz 2002). The accuracy of DES implementations is strongly influenced by the formulation dictating the transition between RANS and LES. In that regard, the DES SST k-ω model applies a delay factor that enhances its ability to distinguish between RANS and LES regions on discretized meshes where ambiguous behavior could arise. More specifically, we implemented in the present application the improved delayed detached eddy simulation (IDDES) formulation (Shura et al. 2008), which applies a RANS-LES hybrid model to use LES when the mesh density allows (where otherwise a standard DES model would always use RANS).

The transport equation (Equation 3.3) for the turbulent kinetic energy (κ) in the Standard SST k-ω model consists of a transient part (first term, LHS), the convection part (second term, LHS), the diffusion part (first term, RHS), and the inclusion of generation and dissipation of the turbulent quantity (D_κ) (second integral in RHS).

$$\frac{d}{dt}\int_V \rho\kappa dV + \int_A \rho\kappa\bar{u}\cdot d\bar{a} = \int_A (\mu+\sigma_k\mu_t)\nabla\kappa\cdot d\bar{a} + \int_V (\gamma_{eff}G_k - D_\kappa)dV \tag{3.3}$$

In the IDDES formulation used in the present work, the dissipation term depends on a hybrid length scale (l_{HYBRID}) as shown below (Equation 3.4):

$$D_k = \frac{\rho\kappa^{3/2}}{l_{HYBRID}} \tag{3.4}$$

The hybrid length scale aims at seamlessly coupling the RANS and LES regions. The full description of l_{HYBRID} is provided by Shura et al. (2008).

3.3 Cases

The solution presented here is the outcome from a number of solutions that iteratively sought to improve the quality of the CFD results. At each iteration, the simulated flow conditions were compared against two LDV data sets available.

- Data set I: Measurements at three bays, at three transects, referred as upstream, middle, and downstream as shown in Figure 3.5.

- Data set II: Vector plots at three transects located at the bay centerline of Bay A (high discharge bay) near the STS structure. The prototype-scaled discharge corresponds to Q = 13.865 kcfs.

The contours and scatter plots for 10 solutions are included in the appendix. In this section, we described the general features of each solution and the reason why we deemed the next iteration necessary.

- Solution 1: This solution was the first approximation with a steady-state RANS simulation of the full unit; i.e., the model contains the three intake bays, the runner, draft tube, etc. The discharge was 14.10 kcfs, slightly higher than the discharge during LDV measurements because this solution targeted a field condition during fish passage studies. The domain was discretized with polyhedral cells.

- Solution 2: Same as Solution 1, but in transient mode (URANS) with ΔT = 0.1 s. The velocity values were interpolated from the instantaneous flow field at time T = 220 s.

- Solution 3: This solution had a reduced domain that accounted only for the high-flow bay (Bay A), with a split discharge of Q_A = 4.99 kcfs. This discharge was selected from the estimates of flow splits from solution 2. It did not include the distributor, runner, and draft tube. To generate the single bay model, the full model was cut before the end of the piers, dividing the intake into three bays. This new outlet was extruded downstream to allow for the exiting flow conditions to fully develop. In the upstream, the reduced inflow upstream from the trashracks was also extruded in the stream-wise direction. The reduced domain was discretized with hexahedral cells. The simulation was a URANS simulation with $\Delta T = 0.1$ s. The velocity values were interpolated from the instantaneous flow field at $T = 360$ s.

- Solution 4: This was essentially the same as Solution 3, but instead of using the instantaneous flow field to interpolate the velocities onto the LDV measurement location, we used the mean velocity field averaged over 2 minutes.

- Solution 5: This was an external solution provided by one of the turbine vendors (Voith) participating in the replacement bids. The model was run as steady-state RANS with the commercial code CFX (Ansys), at a prototype-scaled discharge of 13.63 kcfs for the full model.

- Solution 6: This solution used the same geometry and mesh as in Solution 3, but was run in DES mode as explained in Section 3.2. The velocity values were interpolated from the instantaneous flow field at $T = 90$ s.

- Solution 7: This was essentially the same as Solution 6, but instead of using the instantaneous flow field to interpolate the velocities onto the LDV measurement locations, we used the mean velocity field averaged over 30 s.

- Solution 8: In complex engineering flows, the geometric scaling factors do not necessarily represent the dynamic scaling of turbulent conditions. Because the LDV data were measured in a reduced physical model, this solution was obtained from the *scaled* conditions of geometry and discharge, using the scaling factors of 25 and 3125, respectively. The velocities were interpolated from the mean flow field averaged over a period of 6 s.

- Solution 9: This solution corresponded to the full model configured like Solution 7, but without the runner. All the single-bay solutions (3, 4, 6, 7, and 8) were necessary to test the influence of the turbulence solver (URANS vs DES), the flow field transient state (instantaneous vs. averaged), and the scaling factors (prototype vs. reduced-scale model). In addition, they allowed us to evaluate the effect of cell types (polyhedral vs. hexahedral) and sizes (low vs high mesh density). Full turbine intake solutions are required for fish passage studies. However, the computational time required is prohibitive. Single-bay models were used to evaluate the effects of various modeling selections in a computationally efficient manner. For that reason, Solution 9 uses all of the settings of the single-bay model, but applied to the full model. The only difference with the earlier coarser URANS models (Solution 2) was the lack of the runner geometry and draft tube, because the blades usually require a considerable mesh refinement that will make the current simulations unfeasible.

- Solution 10: This was the same as Solution 9, but instead of using the instantaneous flow field to interpolate the velocities onto the LDV measurement location, we used the mean velocity field averaged over 30 seconds.

Solution 10 provided the results presented in this report. The “No STS” case was developed using the same features and settings used in Solution 10, but without the STS, as was explained in Section 3.1.

4.0 Virtual Current Meter Analysis

4.1 Theory

A VCM array is simulated in the intake bays by sampling the velocity field calculated by the CFD at the proposed VM locations.

The virtual point measurements of the VCM array are used to calculate the discharge through each bay and, in turn, the total intake discharge using the velocity-area method. This method involves the VM of the mean axial flow velocity through a selected plane, and then calculating the volume flow rate as the product of the mean velocity and cross-sectional area of the plane.

The analysis involves the following assumptions:

- The VCM are modeled as a stationary array on a fixed frame that can measure all of the sample locations over the same time frame.
- The VCM are modeled in the flow field of the time-averaged mean velocity calculated as the mean of 30 s of the CFD solution. This duration was observed to be sufficient to remove transient effects from both the mean velocity and mean discharge values.
- The velocity measured by the VCM is equal to the time-averaged velocity at the hub of the current meter rotor.
- The VCM modeled have a diameter of $d = 100$ mm.
- The axes of the VCM are orientated perpendicular to the plane of the instrument array.
- Uncertainty of VM due to the presence of swirl, asymmetry, turbulence, instrument calibration, and installation position and orientation are not considered at this time.

4.2 Locations of Virtual Current Meters

Standards provide recommendations for best practices in the installation of current meters for measuring fluid flow in closed conduits. These standards include PTC-18 (ASME 2011) and IEC-41 (IEC 1991). Both of these standards refer to the requirements of the International Standards Organization (ISO) Standard 3354 (ISO 2008a) for cases where the velocity distribution is regular and the flow is steady. Due to the nature of the short converging intakes and presence of the STS in the intakes at Ice Harbor Dam, these assumptions are invalid. The more complex scenario of current meter measurements in asymmetric and swirling flow conditions is addressed in ISO Standard 7194 (ISO 2008b). This standard is for the flow in circular ducts rather than the rectangular cross section of the intake bays under consideration. Therefore, the VCM analysis presented herein considers a combination of measurement guidelines from both ISO standards, as appropriate.

4.2.1 Virtual measurement sections

Two virtual measurement sections are considered for the VCM performance analysis. The location and justification are described below, and locations are shown in Figure 4.1.

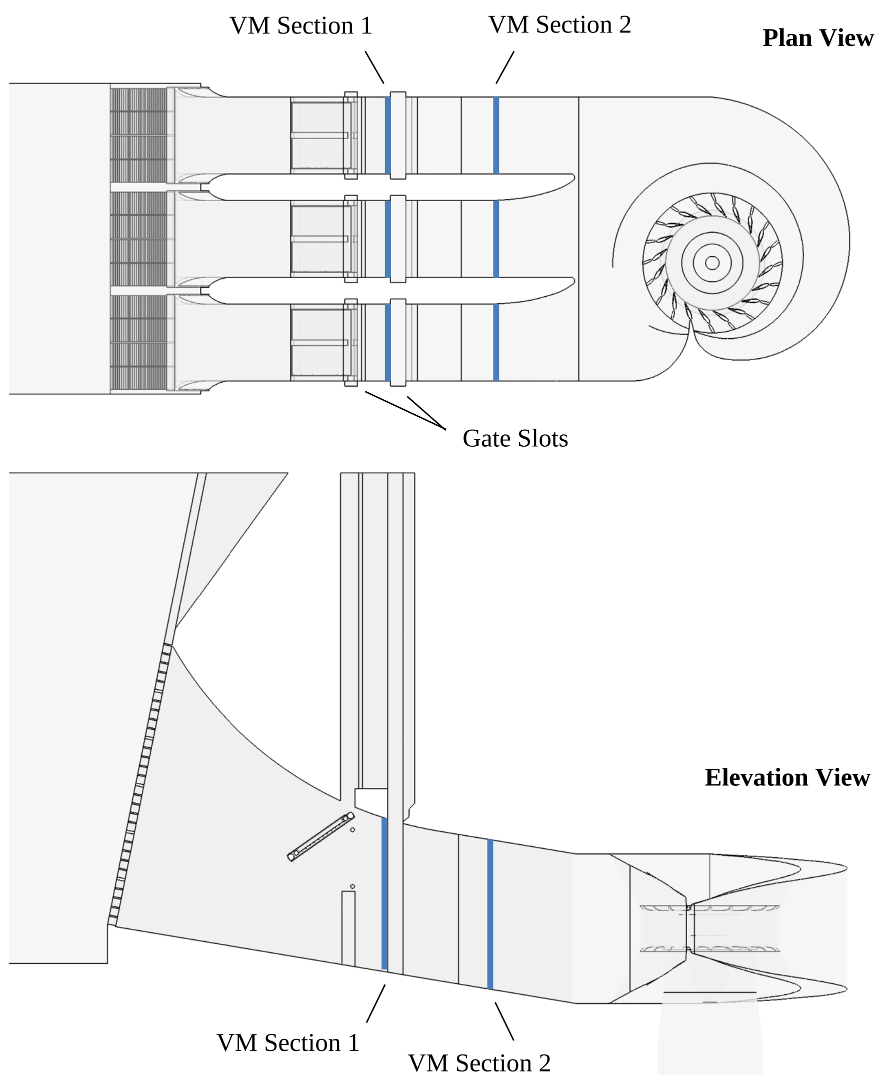

Figure 4.1. Locations of the two VM planes considered in the VCM analysis.

VM Section 1: The first VM section is defined as the upstream face of the second gate slot. This location represents the measurement plane of a pre-assembled array of upstream-facing current meters, deployed down the gate slot, as a practical and cost-effective installation method.

The CFD solution diverts some portion of the flow to the gate well. For this reason, the discharge measured at this section is not the total flow rate, because some flow re-enters the bay through the top of the second gate slot. In the present analysis, the discharge through the VBS, which bypasses VM Section 1 is 4.0% of the total discharge with the STS installed, and 0.4% without. In practice, the flow through the VBS could be prevented, to force all of the flow through this VM plane for the calculation of the total discharge.

VM Section 2: VM Section 2 is defined as the most downstream section of the intake before the three bays begin to converge towards the scroll case. This allows the maximum distance for the flow to develop towards steady and symmetrical profiles. As a result, the rate of shear in the velocity vectors is expected to be at a minimum within each intake bay at VM Section 2.

Although the velocity field is at its most developed state at this location, deployment and maintenance of an instrument array would have significant technical and financial challenges that are avoided by the gate slot deployment of VM Section 1.

The discharges through each VM section were calculated using the CFD visualization and analysis tool Tecplot 360 EX (Tecplot Inc., Bellevue, WA), and are given for each STS configuration in Table 4.1.

Table 4.1. Reference values of the discharge through each VM section for both STS configurations. Inflow to model was 386.9 m^3/s

	Total discharge (m^3/s)	
	STS	No STS
Section 1	371.2	385.2
Section 2	387.0	386.9

4.2.2 Distribution of Virtual Instruments

ISO-3354 prescribes a number of recommendations pertaining to the spacing of current meters and these are also to be followed in ISO-7194, unless otherwise stated. The method of calculating the mean flow to be used in the velocity-area method is also identical between the two standards.

The following guidelines are provided by the industrial standard of ISO-3354 (ISO 2008a) on the acceptable spacing of the current meters from the intake wall and each other:

- A minimum of 25 instruments is required for a rectangular cross section (ISO-3354, Section 4.4.3). This criterion is presented graphically as Exclusion Zone 1 in Figure 4.2.

- A minimum distance of $0.75d$ is required between the outermost current meter and the wall, where d is the diameter of the current meter (ISO-3354, Section 4.4.1). The velocity field in the resulting unmeasured peripheral zone must then be estimated using extrapolation techniques. In the following analysis this minimum separation has been used. The proportion of the total discharge in the peripheral zone for each VM plane and STS configuration is summarized in Table 4.2.

- A minimum distance of $d + 0.03$ m is required between the axes of two adjacent current

Table 4.2. Proportion of the total discharge in the unmeasured peripheral zone for each VM plane and STS configuration

	Proportion of total discharge in peripheral zone (%) STS	No STS
Section 1	3.0	2.7
Section 2	2.6	2.8

meters (ISO-3354, Section 4.4.1). In Figure 4.2, Exclusion Zone 2a and Exclusion Zone 2b denote the minimum separation criterion in the Y-direction and Z-direction, respectively.

- A maximum blockage effect of 6% is acceptable, above which the standard does not apply. This blockage is difficult to quantify in a generalized study because it is a function of the number, profile and frontal area of the support struts, the distance between the rotor plane of the current meter and the support strut, and the type, number, and size of the current meter being modeled (ISO-3354, Section 6.4.3). As such, it has not been considered further in the VCM performance analysis.

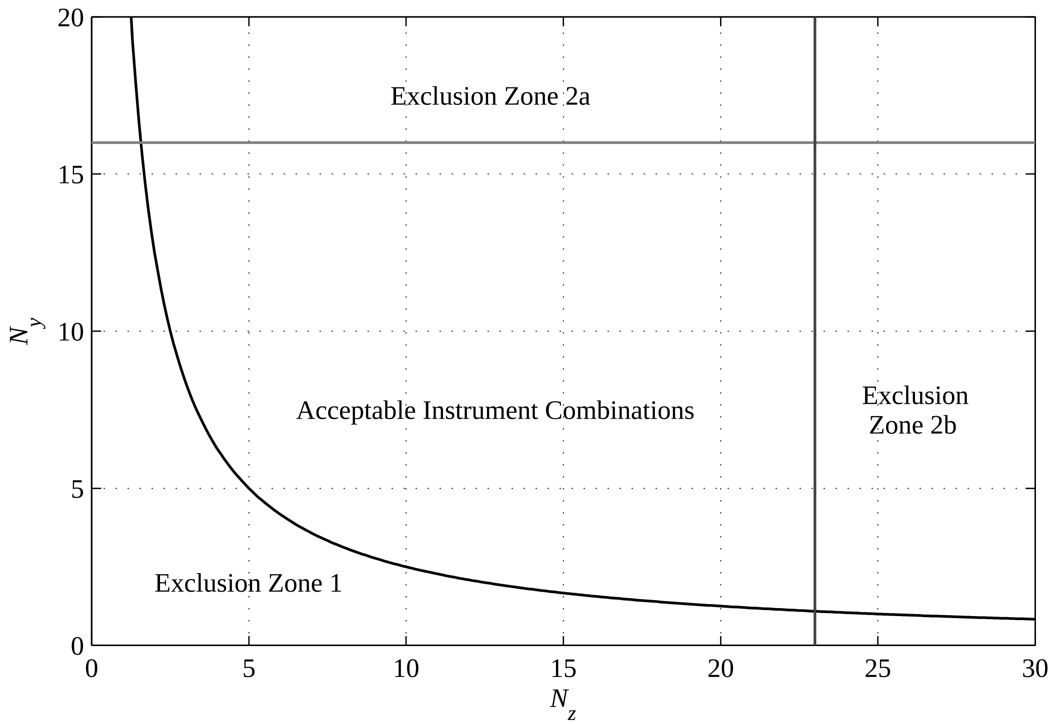

Figure 4.2. Design space for the number of current meters allowable in each direction of the rectangular intake bays at Ice Harbor Dam.

The IEC-41 standard suggests the distribution of measurement locations is highest in zones of steep velocity gradients such that the velocity difference between two adjacent points is minimized (IEC 1991). The maximum shear in the undisturbed flow is at the walls and as such the arrangement of the VCM within the measurable area follows a parabolic distribution, similar to that used in existing flow rate field measurement studies (CEATI 2011). Examples of the parabolic distribution with N_y instruments per row and N_z instruments per column are presented in Figure 4.3. The total number of instruments in the array is denoted as $N_T = N_y \times N_z$.

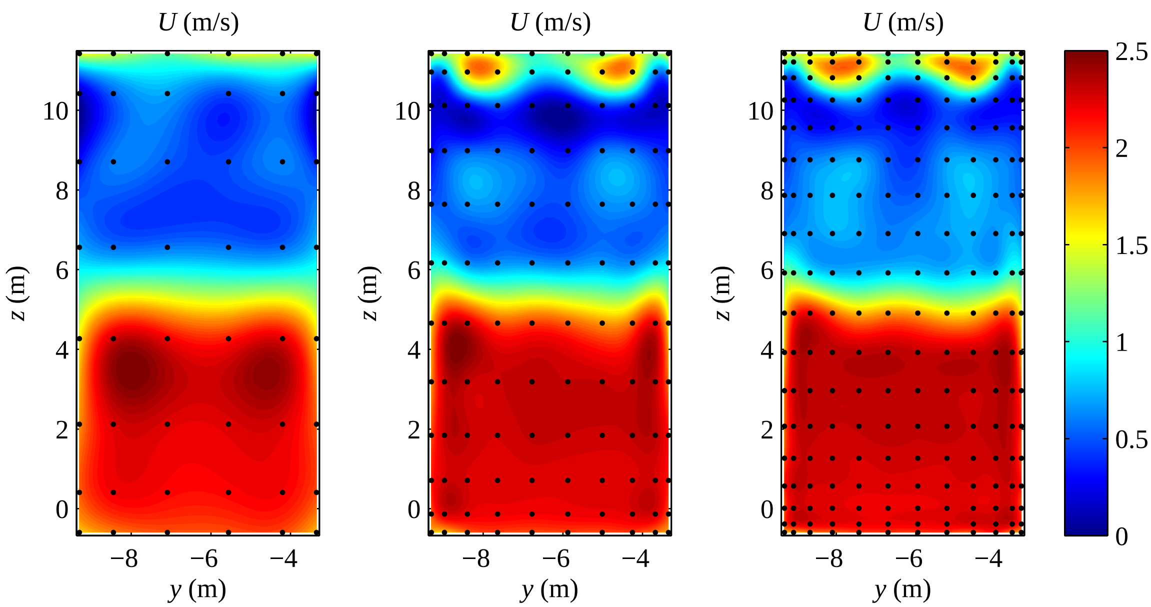

Figure 4.3. Effect of VCM resolution on velocity contours for three $N_y \times N_z$ combinations: 6×8, 10×12, 12×18 (left to right).

The velocity distribution is interpolated between each location sampled by the VCM with a cubic spline interpolation method. While providing a closer approximation of the velocity profile than linear interpolation between VM, the error between the interpolated velocity profiles and those of the CFD solution is shown in Figure 4.4. This error is reduced by increasing the resolution of the VCM in the virtual instrument array.

4.3 Velocity-Area Method

The velocity-area method of determining the discharge through a closed conduit requires the accurate measurement of known locations over a cross section to determine the spatially averaged mean velocity in the direction perpendicular to the measurement plane, U_A. This representative velocity is then multiplied by the cross-sectional area at the plane of the measurements, A, to calculate the discharge rate (Equation 4.1).

$$Q = U_A A = \int_0^1 \int_0^1 \int_0^1 u \frac{\mathrm{d}t}{T} \frac{\mathrm{d}h}{H} \frac{\mathrm{d}l}{L} \tag{4.1}$$

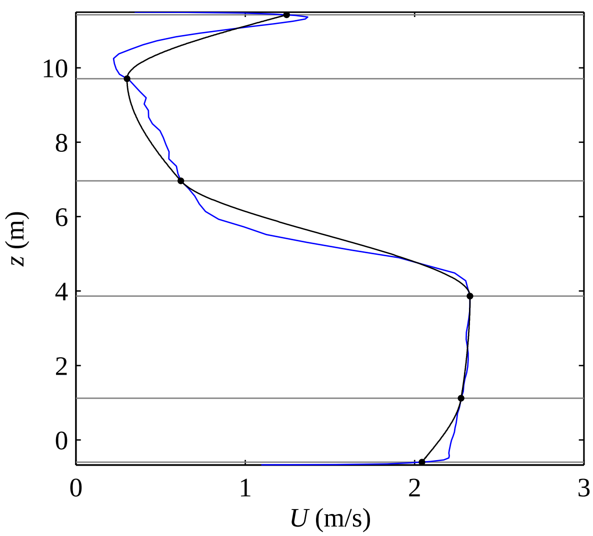

Figure 4.4. Interpolation errors as a result of insufficient vertical sampling resolution. Vertical velocity profiles of the center-line of an individual bay are shown with parabolic sample distribution of $N_z = 6$ (left) and $N_z = 18$ (right). The vertical distribution of the rows of VCM are indicated with gray lines.

Here, T represents the averaging time of the CFD solution, and L and H are the length of the larger and smaller sides of the rectangular cross-section, respectively. The values of l and h represent the distance from the measuring point to the longer and shorter reference wall, respectively. In this analysis, $T = 30$ s, $H = 6.096$ m and $L = 12.169$ m and $L = 11.887$ m at VM Section 1 and VM Section 2, respectively.

The ISO-3354 standard describes three methods of calculating the spatially averaged velocity (ISO 2008a): graphical integration of the velocity area, numerical integration of the velocity area, and arithmetical methods.

In this analysis, the mean axial fluid velocity is determined by graphical integration of the velocity area because it is the most flexible scheme for a wide range of VM locations. This method is described in detail in Section 8.3 of ISO-3354 (ISO 2008a).

With the distance of the outermost VCM being limited to at least $0.75d$ from the intake boundaries, an interpolation must be made to account for the discharge in the unmeasured peripheral zone. This is approximated by assuming that the unmeasured velocity profile follows a power law from the outermost measured point to a value of zero at the wall. This is shown in Equation 4.2, where U_a is the outermost measured velocity, z_{BL} is the distance from the wall to this VM location, a is the width of the unmeasured peripheral zone equal to $0.75d$, and m is the power law coefficient. The value of m is generally in the range of 4–14 with $m = 8$ being appropriate for almost all practical cases (ISO 2008a). This value was observed to be acceptable for the present analysis as shown in the representative case of Figure 4.5.

$$U(z) = U_a \frac{z_{BL}}{a}^{1/m} \quad (4.2)$$

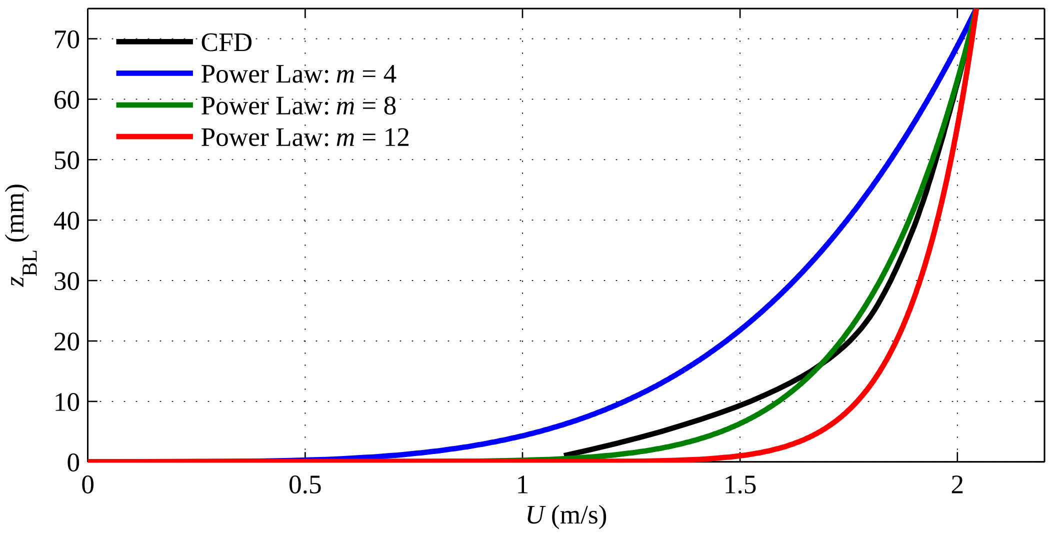

Figure 4.5. Comparison of velocity boundary layer approximations for the range of exponent values (Equation 4.2) with the CFD solution in the vicinity of intake wall.

The VM plane at each of the three intake bays is sampled with an identical VCM array and the velocity-area method is used to calculate the discharge through each bay. The total intake discharge is calculated as the sum of the three individual bays.

5.0 Results and Discussion

5.1 CFD-Simulated Flow Fields

The configuration of STS deployment yields two distinct flow conditions at the turbine intake as shown in Figure 5.1. The resistance of the STS components effectively blocks the flow through the turbine, producing a separated flow region behind the STS that further extends downstream. The remaining flow below the STS and through the upper STS gap is accelerated. In fact, the latter replicates features of a jet injected into a stagnant flow environment. Consequently, the STS configuration exhibits regions with high shear flows that propagate well into the distributor. The presence of these disturbed flows strongly influences the results of fish safety studies conducted with live fish, autonomous sensor devices, or modeling agents, because releases are normally conducted downstream of the STS. The "No STS" configuration shows a contracting flow with less spatial variation than the STS case, and a mild flow acceleration on the top portion of the intake. In addition, the absence of the STS minimized the flow through the gate wells. The averaged velocity fields (Figure 5.1 on the right) reproduce the features of the instantaneous fields. For instance, the jet flow at the upper part of the STS was consistently present during the simulation, whereas the flow into the gate well in the "No STS" configuration was very limited.

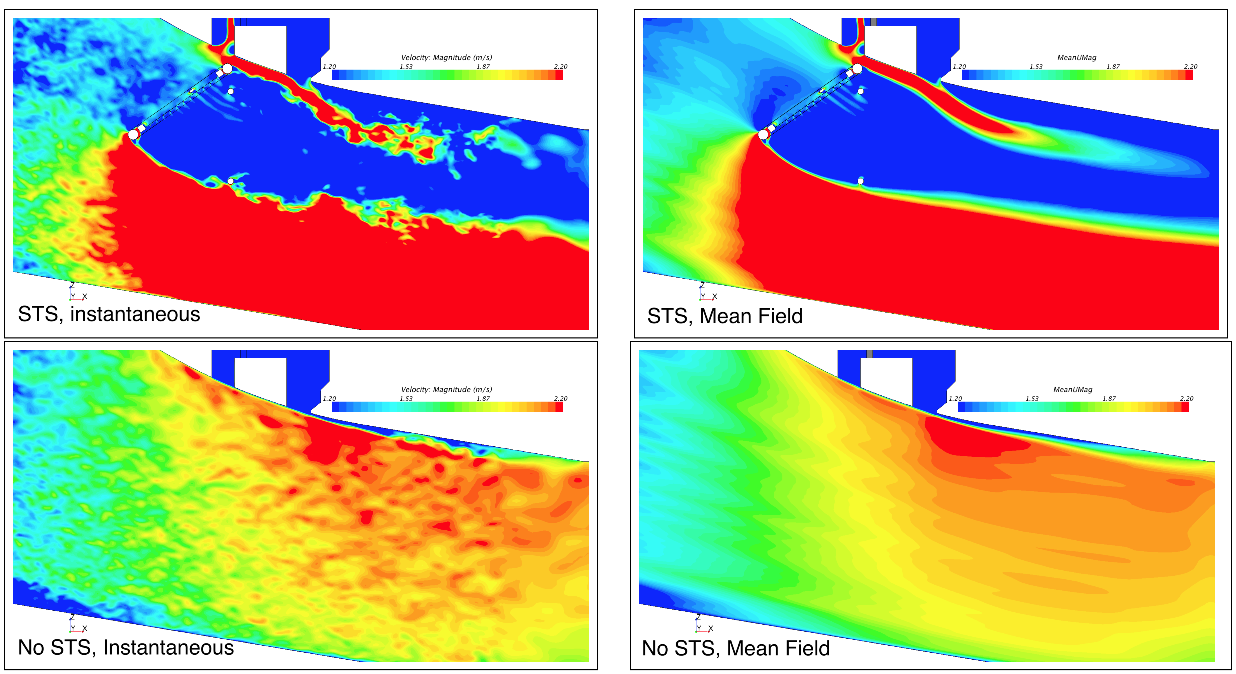

Figure 5.1. Contours of velocity magnitude (in m/s) on a plane at Y = 8.3 m, at the high flow bay (Bay A).

Because the velocity fluctuations are visually manifested, we quantified the levels of turbulent kinetic enegy (TKE) in the two configurations (Figure 5.2). The total TKE is the energy associated with the eddies in a turbulent flow and consists of two portions in a DES simulation: the modeled TKE and the resolved TKE (TKE_{RANS} and TKE_{DES}, respectively, in Equation 5.1), where the root-mean-square (RMS) values are given in Equation 5.2). The random nature of turbulence allowed us to compute the RMS values of each velocity component over the entire spatial domain in post-processing. To that purpose, we applied the statistical relationship in Equation 5.2 that used both the mean of the velocity component ($\bar{u}$), and the mean of the same component to the square, computed each time step ($\bar{u^2}$).

$$TKE_{total} = TKE_{modeled} + TKE_{resolved} = TKE_{RANS} + \frac{1}{2} \cdot (u_{rms}^2 + v_{rms}^2 + w_{rms}^2) \qquad (5.1)$$

$$u_{rms}^2 = \bar{u^2} - \bar{u}^2; v_{rms}^2 = \bar{v^2} - \bar{v}^2; w_{rms}^2 = \bar{w^2} - \bar{w}^2 \qquad (5.2)$$

The contours in Figure 5.2 show the large production of turbulent energy originating from both ends of the STS structure, and stretching until near the start of the distributor. Near and through the distributor, highly energetic levels are present mostly owing to the change in geometry from the intake to the distributor. The STS configuration diverts flow into the gatewell resulting in highly energetic turbulence. The influence of STS on the turbulent environment is almost limited to the downstream direction; both the STS and No STS configurations are visually identical in the region between the trashracks and the STS location. Such turbulent energy from the trashracks is dissipated mainly because of the effect of the contracting flow.

An example of the consequence of the intake turbulence on regions farther downstream is presented with contours of vorticity magnitude on a Z-plane (Figure 5.3). Vorticity is a field that represents the tendency of the flow to spin locally at a point. For reference, the mathematical relationship for the component in Z-direction is given in Equation 5.3. Near the base of the stay vanes and wicket gates (at elevation Z = 2.6 m), the STS configuration resulted in higher levels of instantaneous vorticity magnitude from the incoming flow, compared to the No STS case. The accurate description of hydraulic conditions around stay vanes and wicket gates has been necessary in studies of cyclic loads leading to shear pin damage (Sousa et al. 2009), in the analysis of non-uniform flow fields originating from the vortex shedding frequencies and affecting runner performance (Antonsen, O. 2007), and in the associated hydraulic losses for rehabilitation assessment (Bornard et al. 2014).

$$\varpi_z = \frac{\partial v}{\partial x} - \frac{\partial u}{\partial y} \qquad (5.3)$$

Figures 5.4 and 5.5 show the velocity profiles in the vertical direction from both the LDV data sets and CFD results. In each figure, two velocity components (stream-wise and vertical) are plotted for each transect location shown in Figure 3.5 (2 components $\times$ 3 transects = 6 plots). Each plot is composed of five subplots corresponding to the vertical rows in each transect, colored by "Line" in Figure 3.5. Each subplot, in turn, contains three data sets: the LDV measurements, the STS, and the "No STS" results. In this way, each subplot seeks to show two features: 1) the agreement between laboratory and CFD results (both conducted in "STS" configuration)

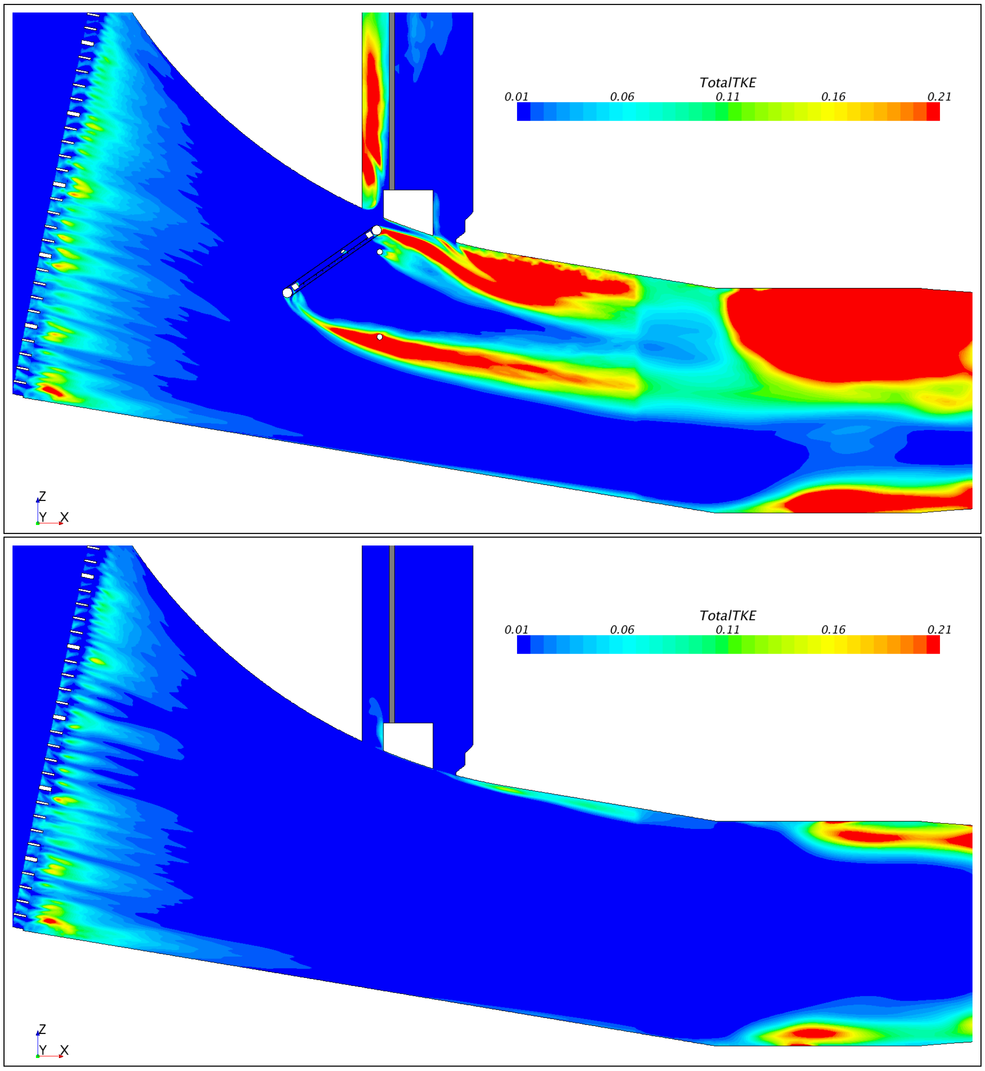

Figure 5.2. Contours of total turbulent kinetic energy (in m^2/s^2, as in Equation 5.1) on a plane at Y = 8.3 m, at the high flow bay (Bay A), with STS (top) and without STS (bottom).

and 2) the contrast between STS and "No STS" configurations (available from CFD but not from LDV data sets). The lower and upper limit of the velocity value is indicated in the first subplot and applies to all.

For the case of mean velocities (Figure 5.4), the comparisons between the LDV data and the STS results exhibit an acceptable level of agreement. Because of the contracting geometry of the intake, stream-wise velocities (U) mostly decrease with elevation, and vertical velocities (W) are mostly negative. The blockage effect of the STS is manifest by the acceleration of flow at the lower half of the plots in the middle transect. The LDV and CFD profiles at the downstream transect capture the jet-like flow originating from the upper end of the STS (discussed in Section 5.1 and shown in Figure 5.1). The presence of the jet is observed as a "hump" in the curves

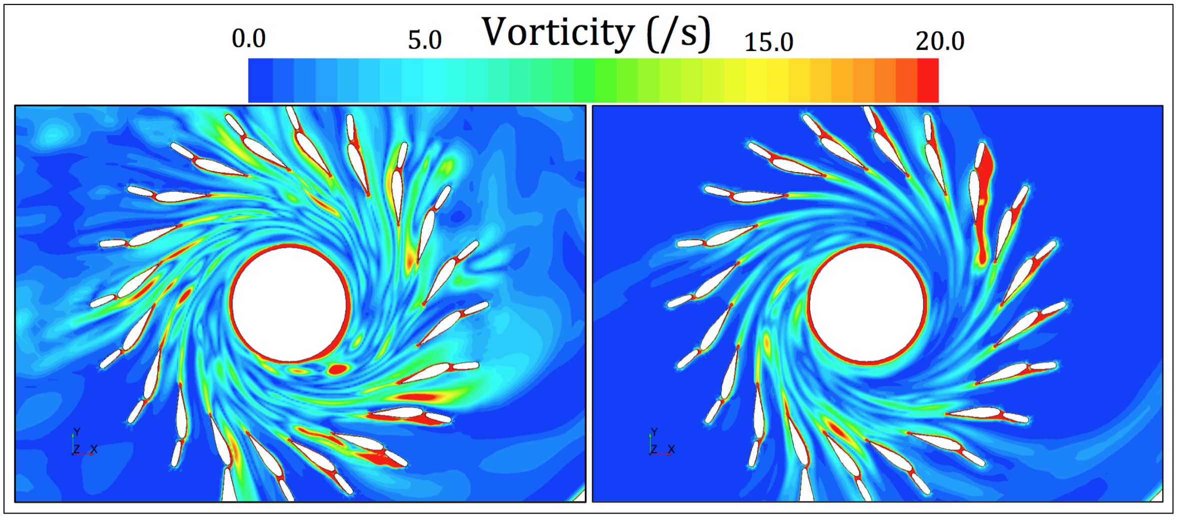

Figure 5.3. Contours of instantaneous vorticity magnitude (in s^{-1}) on a plane at Z = 2.6 m.

for Z values greater than 5 m. However, the CFD results appear to be consistently offset by +0.5 m in comparison to the LDV data. The offset likely stems from underlying assumptions of the DES approach to model flow on the upper wall. All curves from the "No STS" configuration eliminate the large vertical variability and make the curves look more uniform than in the STS case, except at the top and bottom of the subplots where the influence of the wall boundary is stronger.

For the case of RMS velocities (Figure 5.5), we observed poor agreement between CFD results and LDV data in the STS configuration for the upstream and middle transects. Although both the field data and numerical results yield consistent spatial fluctuations in the vertical direction, the CFD results exacerbate the range considerably. In addition, all of the CFD curves are underestimated. This derives from a number of possible reasons. First, the geometric representation of the trashracks in the CFD model lacks the vertical support bars that were present during the laboratory runs, which could be contributing to the shear generation. Second, DES formulation includes a number of coefficients and parameters that are empirically calibrated in simpler canonical flows; using them for a complex engineering flow of the present scale may contribute to the deviations observed herein. Lastly, the incoming turbulent condition in the laboratory is assumed to be low and the turbulent intensity was set at 1% in the present simulations; however, the actual value may also contribute to the discrepancies in the upstream and middle transects. The downstream transect, on the other hand, exhibits a very high correlation between the LDV measurements and numerical results. Similar to the trends in the mean velocities, there is an offset between the curves in the portion corresponding to the upper jet flow.

The RMS curves in the "No STS" configuration exhibit the expected tendency of decreasing turbulent fluctuations in a contracting flow with no significant blockage effect. Notice that the subplot scale is reduced from the upstream (0.00 to 0.20 m/s) to the middle (0.00 to 0.13 m/s) transect to depict such reduction in RMS. Although the scale increases for the downstream transect to include the curves from the STS configuration, the RMS values are considerably low at that stage.

Overall, the quality of the CFD results suffices to supply the hydraulic conditions upon which the subsequent analyses of VMC are conducted. Statistical measures of the present and other solutions listed in Section 3.3 are provided in the Appendix. The solution on which the subsequent VCM analysis was conducted corresponds to Solution 10. The deviations were measured in terms of a statistical correlation (R^2) and mean absolute error (MAE), with values of 0.792 and 0.137 m/s for Solution 1, respectively (see Sections 3.3 and the Appendix for explanation).

The placement of the VCM favors regions with low flow distortion and flow away from large structures. It will be shown that the most reliable location for the following analysis lies between the gate slots and distributor, where the best agreement between the laboratory measurements and modeling results is found.

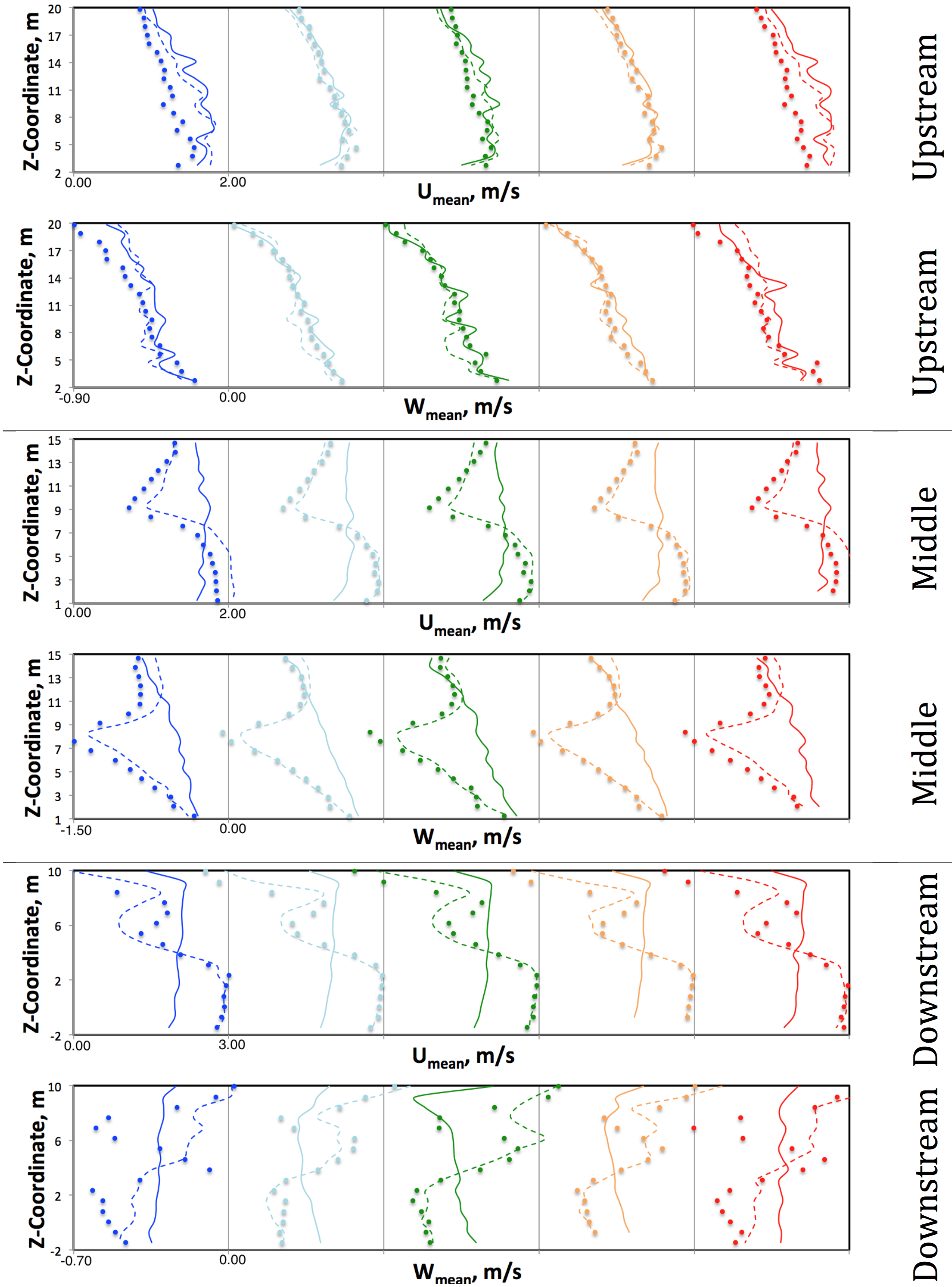

Figure 5.4. Comparisons of mean velocities between LDV data (filled circles) and CFD results from the configuration with the STS (dashed line) and without the STS (continuous line). Only data for Bay A are included. Color coding as in Figure 3.5.

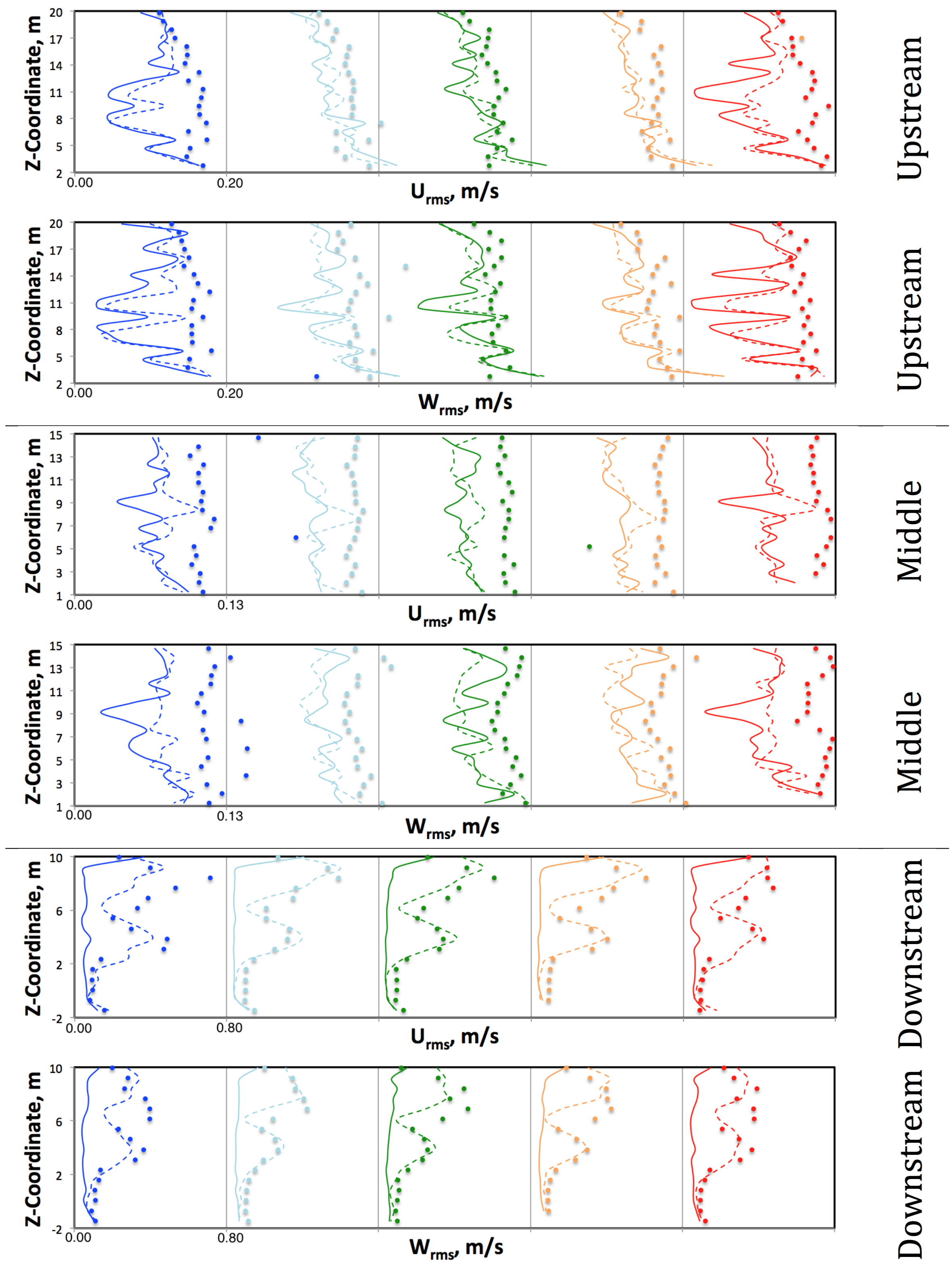

Figure 5.5. Comparisons of RMS velocities between LDV data (filled circles) and CFD results from the configuration with the STS (dashed line) and without the STS (continuous line). Only data for Bay A are included. Color coding as in Figure 3.5.

5.2 Virtual Current Meters

The VCM velocities were extracted from the CFD solution of the mean flow component perpendicular to the VM plane. This was performed at both VM sections, with and without the STS, for each configuration of the VCM array.

The discharge was calculated using the graphical integration solution to the velocity-area method and compared with the reference discharge for each scenario presented in Table 4.1. The relative discharge error, e_Q, between the value calculated using the VCM analysis, Q_{VCM}, and the reference value, Q_0, and calculated using Equation 5.4.

$$e_Q = 100(Q_{\mathrm{VCM}} - Q_0)/Q_0\% \tag{5.4}$$

An iterative analysis was performed for all combinations of $2 < N_y < 16$ and $2 < N_y < 23$, although a number of the resulting combinations were outside of the design envelope of Figure 4.2. The discharge and the relative discharge error were then calculated for each VCM array configuration. The results are shown in the contour plots of Figure 5.6. Results for the array configurations that did not comply with the design envelope are not included in these plots.

The discharge error was observed to be greater than $\pm$ 5% for array configurations with less than five current meters in either rows or columns, for both VM sections and STS configurations.

A diminishing fluctuation in the discharge error in response to increasing N_z was observed for both VM sections where the STS was present. The STS introduces a significant asymmetry in the flow around a horizontal axis making the discharge highly sensitive to the VCM positioning scheme. As the number of instruments in the vertical direction is increased, the sample locations of each row are altered. For example, as the number of rows is increased from $N_z = 4$ to $N_z = 5$, the location of every row is adjusted. This significantly adjusted the velocity profile that is estimated by the spline interpolation between the measured points. While the instrument arrays are relatively sparse, this results in an observable fluctuation in the calculated discharge.

The results shown in Figure 5.6 were used to deduce the minimum number of VCM required to calculate a relative discharge error below a range of acceptable error thresholds, $e_{Q,\max}$. The results are shown in Figure 5.7 to examine the effect of the VM section and STS.

When the STS is present, a greater number of VCM are required to achieve the same relative VM error at VM Section 1 when compared with VM Section 2 for nearly all values of $e_{Q,\max}$. As previously discussed, the STS introduces significant flow disturbances and vertical asymmetry, and causes large changes in velocity within the VM area. The velocity shear introduced by the STS is reduced by the downstream location of VM Section 2 through the process of turbulent mixing. Therefore, fewer instrument are required to characterize the velocity profile to an equivalent level of accuracy.

For the case where the STS is not present in the CFD model of the intake, the flow condi-

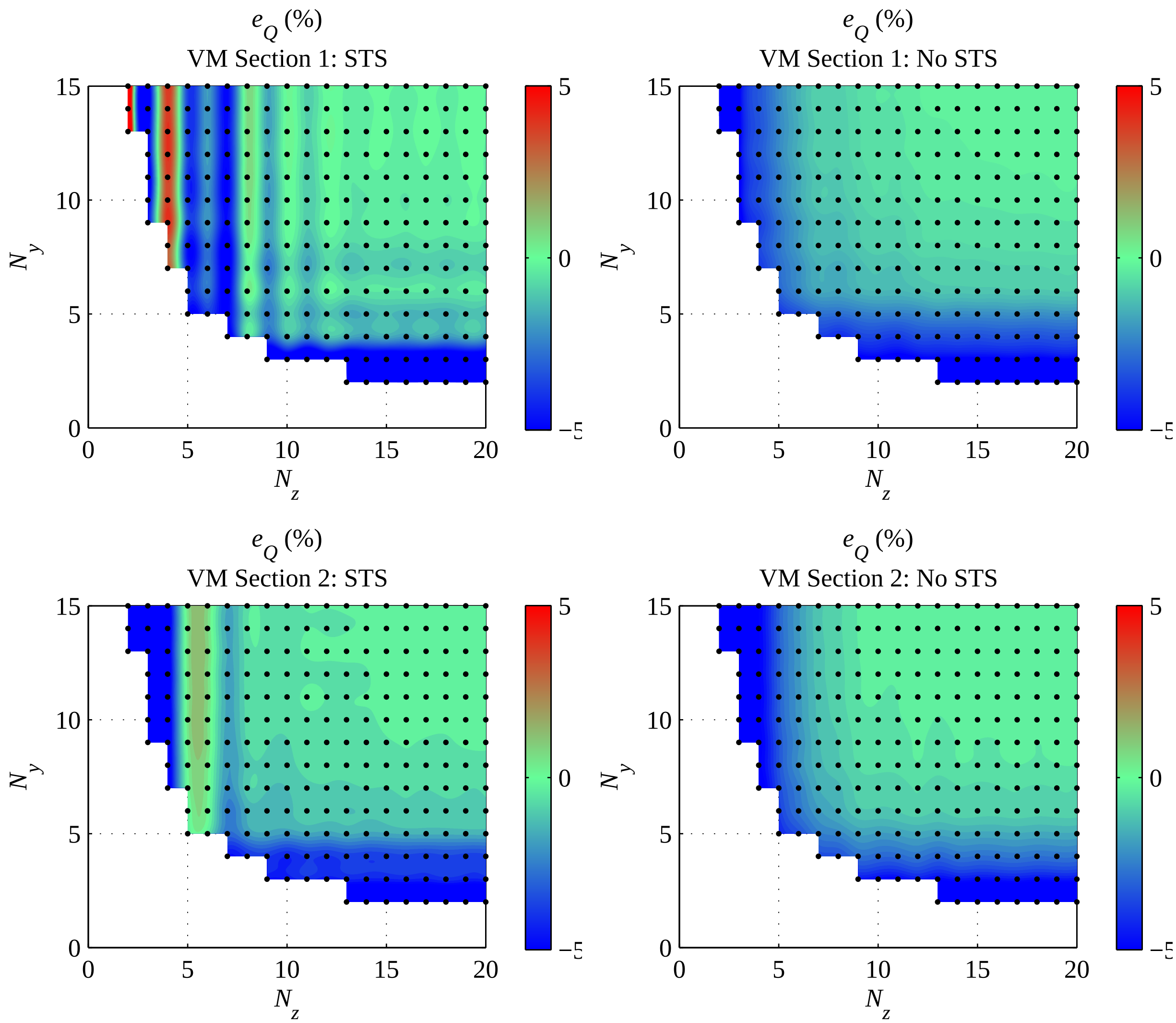

Figure 5.6. Comparisons of discharge error as a function of the number of instrument in the horizontal direction, N_y, and vertical direction, N_z.

tions between VM Section 1 and VM Section 2 are much more comparable. This is reflected in the similar number of instruments required to measure the discharge value to an error of $1.5\% \leq e_{Q,\max}$. The significance of the VM location increases when higher accuracy discharge calculations required; the the upstream location of VM Section 1 requiring significantly more instruments than VM Section 2 to achieve errors of $e_{Q,\max} \leq 1\%$.

Due to the non-permanent nature of the STS, it is important to explore the combined performance of an array configuration both with and without the STS being installed. To this end, the instrument configuration that satisfied the discharge error threshold with the minimum number of instruments for both STS configurations was calculated for each VM section. The results are shown in Table 5.1 with the added constraint of $N_T \geq 25$.

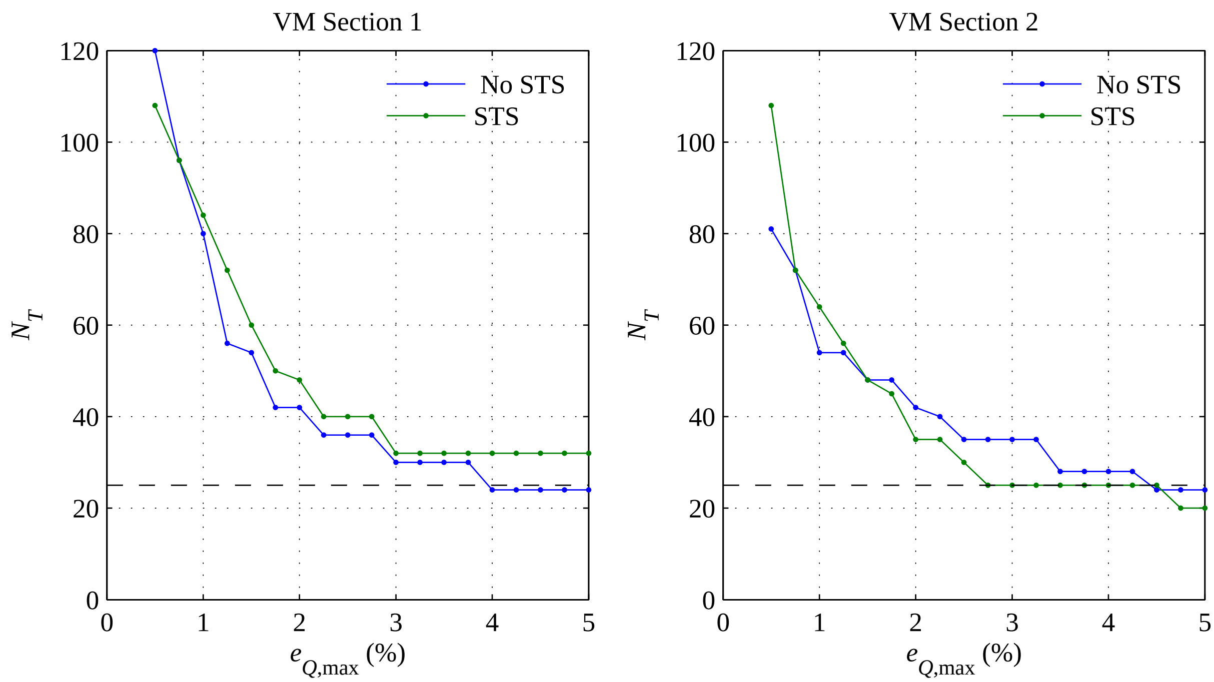

Figure 5.7. Number of VCM, N_T, required to calculate a discharge within an acceptable relative error threshold, $e_{Q,\max}$. The results for the CFD simulations at VM Section 1 and VM Section 2 are shown in the left and right hand plots, respectively. The threshold of the minimum number of instruments required by ISO-3354 ($N_T \geq 25$) is shown with a dashed black line.

Table 5.1. Suggested VCM configurations for a range of acceptable error thresholds (no STS).

$e_{Q,\max}$	VM Section 1			VM Section 2		
	N_y	N_z	N_T	N_y	N_z	N_T
5%	4	8	32	5	5	25
2%	4	12	48	6	7	42
1%	6	14	84	8	8	64
0.5%	12	10	120	9	12	108

The number of instruments required at VM Section 1 is consistently greater than that at VM Section 2 for the same relative error threshold. By locating the array at the downstream location, 11–33% fewer instruments are required than at the second gate slot for a given tolerance level of discharge error.

6.0 Summary and Future Work

An array of VCM was modeled in the mean velocity field calculated by the CFD simulation. The CFD solution adopted for the VCM analysis was developed through a number of iterations to improve the model agreement with LDV data, particularly the correlation to velocity fluctuations. For that purpose, the CFD flow field was computed with a DES. Although computationally more costly than the standard RANS-based CFD flows, the eddy-resolving strategy allowed us to gain confidence for relying on the numerical results for the VCM portion of the work.

The velocity data extracted at the VCM locations were used to calculate the discharge through each intake bay using the velocity-area method. A sensitivity study was performed to observe the effect of array resolution on the discharge error. The analysis was performed for two array locations in the intake; at the second gate slot (VM Section 1) and at the downstream end of the constant cross-section portion of the intake (VM Section 2). The effect of the flow disturbance in the wake of the STS on the discharge error was also observed.

Suggested array configurations for a number of discharge error thresholds are presented. The number of instruments required to achieve a given level of discharge error is greater for the upstream VM location because the larger flow disturbance in the immediate wake of the STS. For example, a total of 84 instruments were required to achieve a relative discharge error of $e_Q = 1\%$ at VM Section 1, which is reduced to a requirement of 64 instruments when the array is positioned at VM Section 2.

Future analyses of the virtual instrumentation described herein could include the following:

- Temporal effects. The effects of the unsteady flow conditions may be modeled by using the velocity field calculated by the CFD at each time step; this can be used to increase the understanding of the dynamic flow effects on discharge estimation.

- Additional velocimetry techniques. Although the scope of this report was limited to virtual propeller-type current meters, the high spatio-temporal resolution of the CFD solution allows such techniques as acoustic scintillation and ultrasonic measurement techniques to be modeled.

- Optimization of the VCM array spacing. The algorithm for the VCM spacing was standardized in the analysis in this report. The number of virtual instruments were distributed between the boundaries of the measurable section with a parabolic distribution in both the rows and columns. This predetermined array distribution is likely to be sub-optimal for capturing the behavior of the flow distribution throughout the measurement section. The positioning of the instruments is of particular importance when the VCM array is sparse and the optimization of these sample locations will be investigated in future analyses.

7.0 References

Antonsen, O.. 2007. *Unsteady flow in wicket gate and runner with focus on static and dynamic load on runner*. PhD thesis, Norwegian University of Science and Technology.

ASME. 2011. "Hydraulic Turbines and Pump-Turbines: Perfomance Test Codes." *American Society of Mechanical Engineers (ASME) PTC 18-2011*.

Bornard L, F Debeissat, Y Labrecque, M Sabourin, and L Tomas. 2014. "Turbine hydraulic assessment and optimization in rehabilitation projects." In *Proceedings of the 27th IAHR Symposium on Hydraulic Machinery and Systems*. International Association for Hydro-Environment Engineering and Research. Montreal, Canada.

CD-adapco. 2014. *User Guide, STAR-CCM+ Version 9.04*. CD-adapco, http://www.cd-adapco.com.

CEATI. 2011. *Short Converging Intake Comparative Flow Rate Measurement Tests at Kootenay Canal*. Report No. T092700-0358, CEATI International, Quebec, Canada.

Christian M, K Lee, B Smith, and B Hadjerioua. 2015. "Impact of the Number of Applied Current Meter Sensors on the Accuracy of Flow Rate Measurements across a Range of Hydroelectric Facilities Indicative of the Domestic Hydroelectric Fleet." In *HydroVision 2015: Proceedings of the HydroVision International Conference*. Portland, Oregon.

Harding S, M Richmond, P Romero-Gomez, and J Serkowski. 2016. "Effects of non-homogeneous flow on ADCP data processing in a hydroturbine forebay." *Flow Measurement and Instrumentation* In press.

Hellström JGI, BD Marjavaara, and TS Lundström. 2007. "Parallel CFD Simulations of an Original and Redesigned Hydraulic Turbine Draft Tube." *Advances in Engineering Software* 38(5):338–344.

IEC. 1991. "Field acceptance tests to determine the hydraulic performance of hydraulic turbines, storage pumps and pump-turbines." *International Electrotechnical Commission (IEC) 41*.

ISO. 2008a. "Measurement of clean water flow in closed conduits – Velocity-area method using current-meters in full conduits and under regular flow conditions." *ISO 3354*.

ISO. 2008b. "Measurement of fluid flow in closed conduits – Velocity-area methods of flow measurement in swirling circular ducts by means of current-meters or Pitot static tubes." *ISO 7194*.

Khan L, E Wicklein, M Rashid, L Ebner, and N Richards. 2004a. "Computational fluid dynamics modeling of turbine intake hydraulics at a hydropower plant." *Journal of Hydraulic Research* 42(1):61–69.

Khan LA, EA Wicklein, M Rashid, LL Ebner, and NA Richards. 2004b. "Computational fluid dynamics modeling of turbine intake hydraulics at a hydropower plant." *Journal of Hydraulic Research* 42(1):61–69.

Lee K, M Christian, and B Smith. 2015. "Development and application of a standardized flow measurement uncertainty analysis framework to various low-head short-converging intake types across the United States federal hydropower fleet." In *HydroVision 2015: Proceedings of the HydroVision International Conference*. Portland, Oregon.

Maruzewski P, H Hayashi, C Munch, K Yamaishi, T Hashii, HP Mombelli, Y Sugow, and F Avellan. 2010. "Turbulence modeling for Francis turbine water passages simulation." *IOP Conference Series: Earth and Environmental Science* 12(1):012070.

Menter F and M Kuntz. 2002. "Adaptation of Eddy Viscosity Turbulence Models to Unsteady Separated Flows Behind Vehicles." *The Aerodynamics of Heavy Vehicles: Trucks, Buses and Trains*, McCallen, R. and Browned, F. and Ross, J., ed. Springer, Asilomar, California.

Nennemann B, T Vu, and M Farhat. 2005. "CFD prediction of unsteady wicket gate-runner interaction in Francis turbines: A new standard hydraulic design procedure." In *HYDRO 2005 International Conference and Exhibition*. October 2005, Villach, Austria.

Prasad V. 2012. "Numerical simulation for flow characteristics of axial flow hydraulic turbine runner." In *2nd International Conference on Advances in Energy Engineering (ICAEE)*, Zeng, D., ed., Vol. 14 of *Energy Procedia*, pp. 2060–2065. Asia Pacific Human-Comp Interact Res Ctr. 2nd International Conference on Advances in Energy Engineering (ICAEE), Bangkok, Thailand, December 27–28, 2011.

Richmond M, S Harding, and P Romero-Gomez. 2015. "Numerical performance analysis of acoustic Doppler velocity profilers in the wake of an axial-flow marine hydrokinetic turbine." *International Journal of Marine Energy* 11:50–70.

Roh HW, SH Suh, Jh Jung, and S Oh. 2010. "Development of a high performance Francis turbine for runner replacement using a CFD-based design system." In *Proceedings of the ASME Fluids Engineering Division Summer Conference - 2010 - Vol 1, PTS A-C*, pp. 843–848. ASME, Fluids Engineering Division. Third Joint US-European Fluids Engineering Division Summer Meeting, Montreal, Canada, August 01–05, 2010.

Shura M, P Spalart, M Strelets, and A Travin. 2008. "A hybrid RANS-LES approach with delayed-DES and wall-modelled LES capabilities." *International Journal Heat and Fluid Flow* 29(6):1638–1649.

Sousa F, L Noleto, A Diniz, and A Brasil Jr. 2009. "Hydrodynamic loads on a hydraulic turbine wicket gate." In *Proceedings of 20th International Congress of Mechanical Engineering*. Associação Brasileira de Engenharia e Ciências Mecânicas. November 15-20, Gramado, Brazil.

USBR. 2006. *Fish Protection at Water Diversions: A Guide for Planning and Designing Fish Exclusion Facilities*. U.S. Bureau of Reclamation, Denver, Colorado.

Wu J, K Shimmei, K Tani, K Niikura, and J Sato. 2007. "CFD-based design optimization for hydro turbines." *Journal of Fluids Engineering-Transactions of the ASME* 129(2):159–168.

Appendix

1. List of solutions and general settings

Table 1. General information of solution settings

Solution	Organization	Domain	Turbulence Approach	Discharge kcfs (bay A)	Time solution	Note
1	PNNL	Full unit	RANS	14.10 (5.06)	Steady	-
2	PNNL	Full unit	URANS	14.11 (5.05)	Transient	Instantaneous flow field
3	PNNL	Single bay	URANS	4.99	Transient	Instantaneous flow field
4	PNNL	Single bay	URANS	4.99	Transient	Mean flow field
5	Voith	Full unit	RANS	13.63 (4.89)	Steady	CFX solution
6	PNNL	Single bay	DES	4.99	Transient	Instantaneous flow field
7	PNNL	Single bay	DES	4.99	Transient	Mean flow field
8	PNNL	Single bay	DES	0.0016 (scale)	Transient	Physical model size
9	PNNL	Full unit	DES	13.66	Transient	Instantaneous flow field
10	PNNL	Full unit	DES	13.66	Transient	Mean flow field

2. Presentation of results

The CFD results were compared against two datasets of experimental measurements available from a physical model

- Dataset I: Measurements at three bays, at three transects, referred as upstream, middle and downstream as shown in Figure 3.5
- Dataset II: Vector plots at three transects located at bay centerline of bay A (high discharge bay), near the STS structure. The scaled discharge corresponds to Q = 13.865 kcfs

Table 2. Material presented from CFD solutions

Chart type	Data source	Comments
3D vector plots in Bay A	I	ERDC data in blue CFD data in red
2D vector plots in Bay A	I	ERDC data in blue CFD data in red
Scatter plots of velocity magnitude all bays	I	Upstream in blue Middle (near STS) in green Downstream in red
Scatter plots of TKE all bays	I	Upstream in blue Middle (near STS) in green Downstream in red
Contours of velocity magnitude Bay A	II	-
2D vector plots near STS	II	ERDC on background figure CFD data in red
Scatter plots of velocity magnitude near STS	II	-

2. Statistics

Table 3. Mean Absolute Error (in m/s) of velocity magnitude from all CFD solutions based on Dataset I

Sample	Sol2	Sol 3	Sol4	Sol5	Sol6	Sol7	Sol8	Sol 9	Sol10
Pooled	0.178	0.142	0.138	0.175	0.186	0.157	0.125	0.187	0.161
Upstream	0.090	0.144	0.143	0.100	0.162	0.133	0.125	0.141	0.107
Middle	0.075	0.081	0.083	0.116	0.103	0.086	0.083	0.084	0.074
Downstream	0.398	0.207	0.196	0.329	0.307	0.266	0.172	0.357	0.322

Table 4. Correlation (R^2) of velocity magnitude from all CFD solutions based on Dataset I

Sample	Sol2	Sol 3	Sol4	Sol5	Sol6	Sol7	Sol8	Sol 9	Sol10
Pooled	0.722	0.923	0.923	0.814	0.810	0.868	0.921	0.746	0.792
Upstream	0.679	0.400	0.402	0.630	0.360	0.432	0.429	0.511	0.636
Middle	0.953	0.941	0.939	0.932	0.915	0.941	0.949	0.925	0.949
Downstream	0.603	0.937	0.949	0.746	0.768	0.846	0.922	0.662	0.719

Table 5. Summary of comparisons to ERDC data based on Dataset II

Solution	R^2	MAE (m/s)
1	0.921	0.221
2	0.926	0.216
3	0.961	0.180
4	0.966	0.169
5	0.925	0.195
6	0.942	0.189
7	0.958	0.169
8	0.957	0.031 (0.155 Scaled up)
9	0.903	0.189
10	0.962	0.137

SOLUTION 2

Dataset I

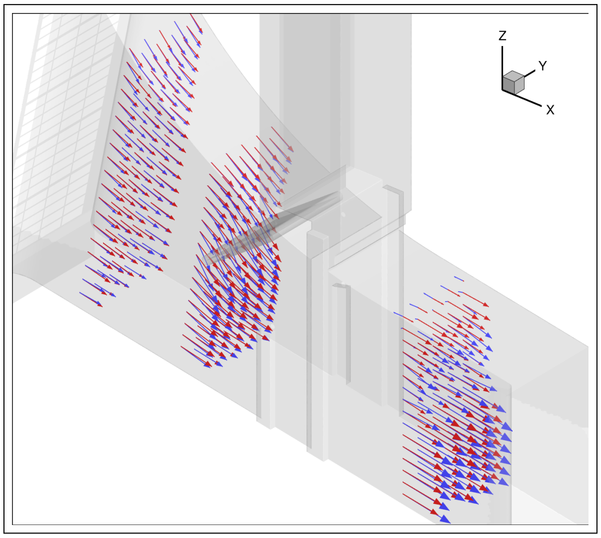

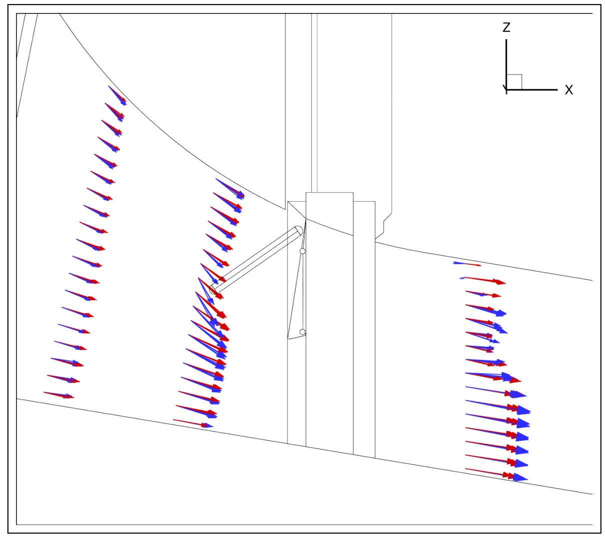

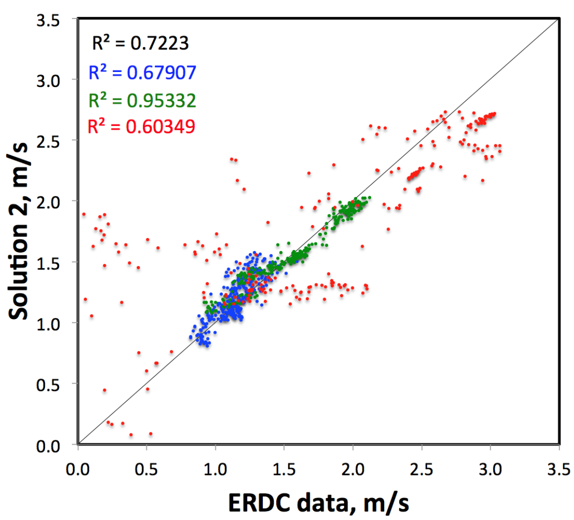

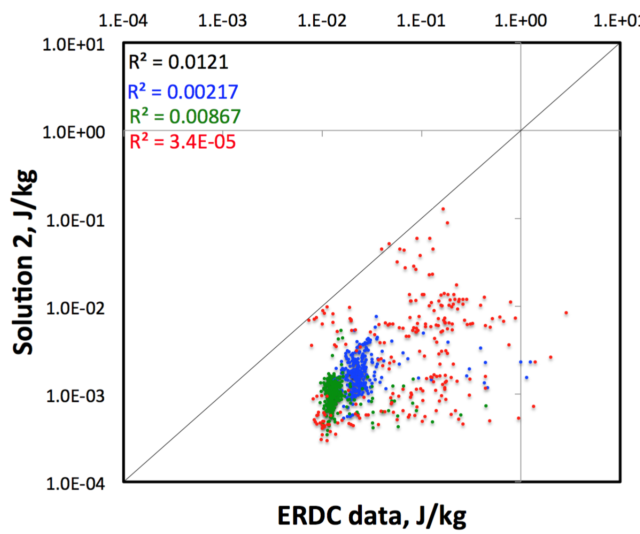

Dataset II

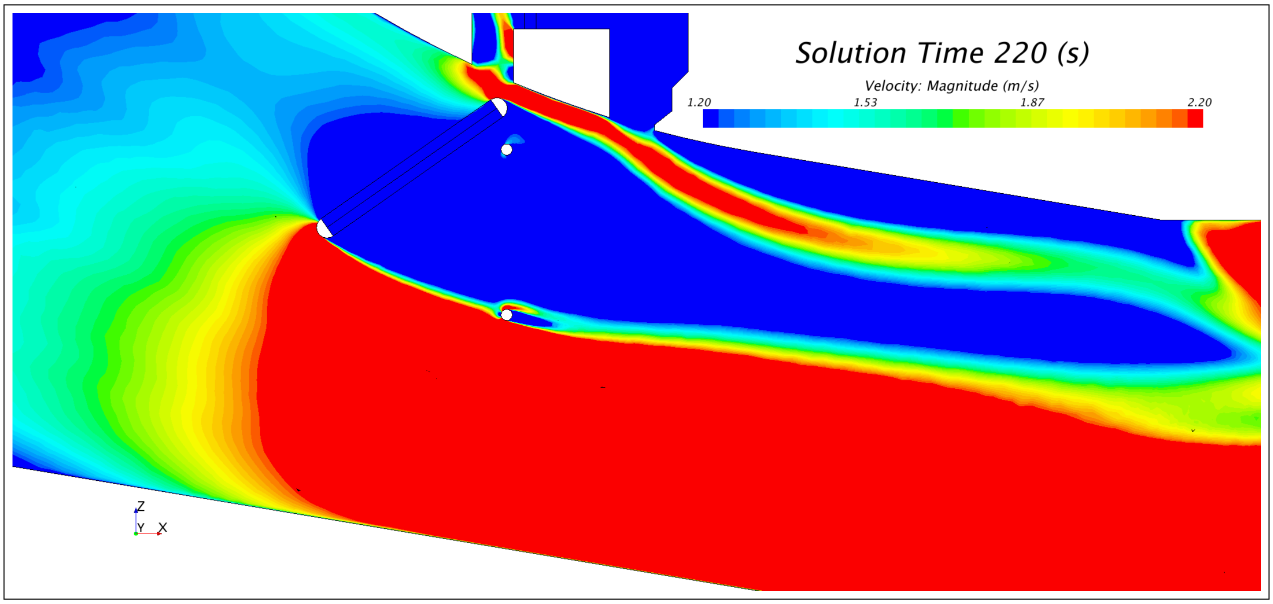
Solution Time 220 (s)
Velocity: Magnitude (m/s)
1.20
1.53
1.87
2.20

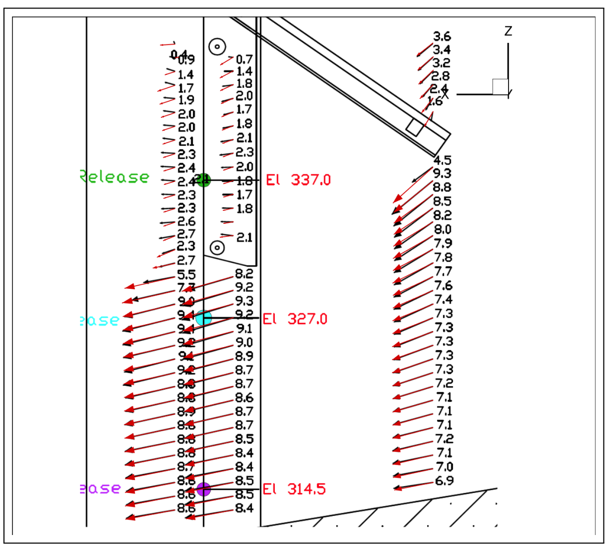
El 337.0
El 327.0
El 314.5

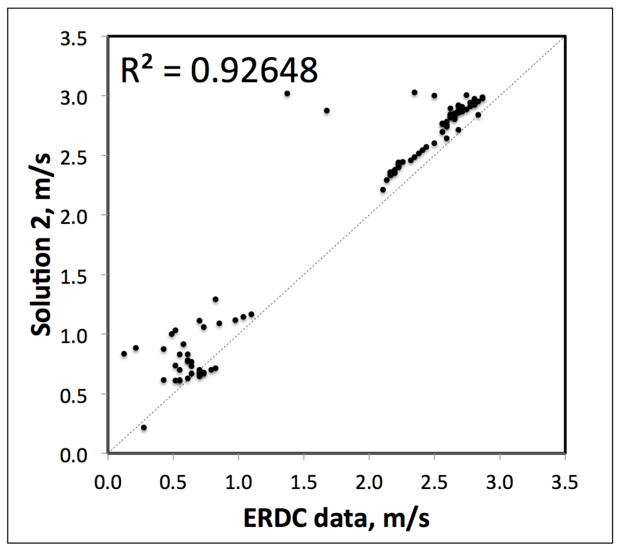
$R^2 = 0.92648$
Solution 2, m/s
ERDC data, m/s

SOLUTION 3

Dataset I

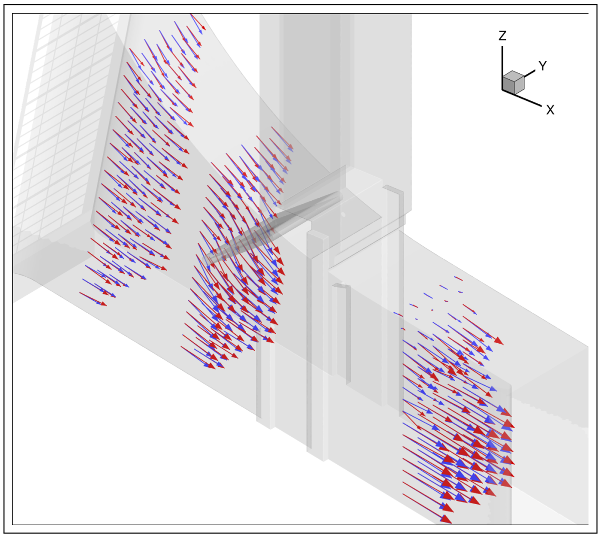

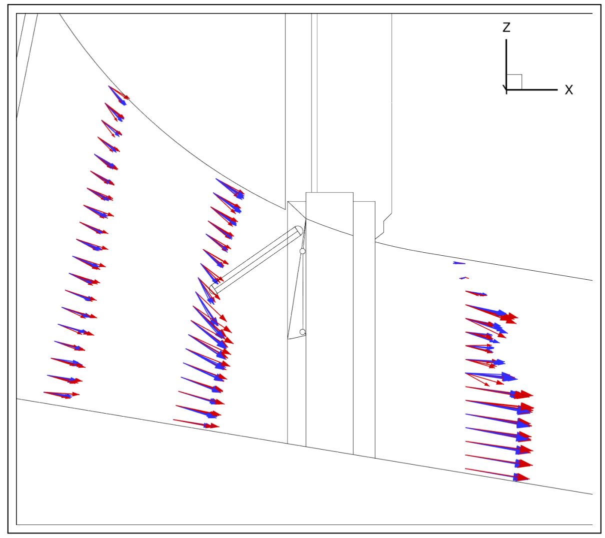

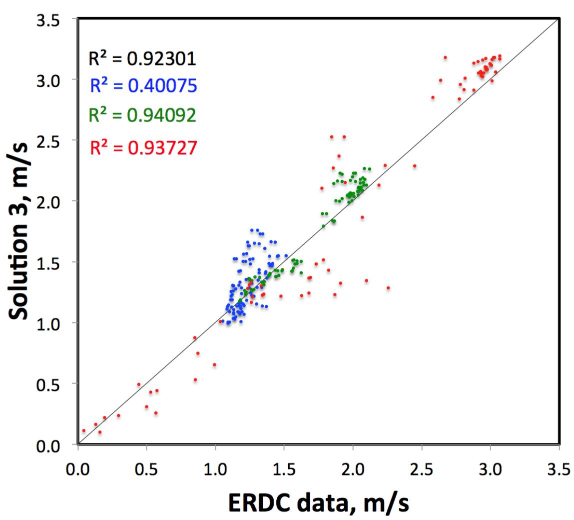

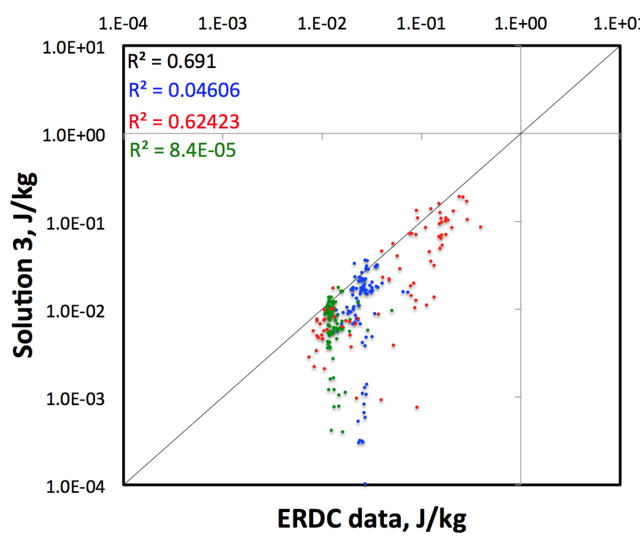

Dataset II

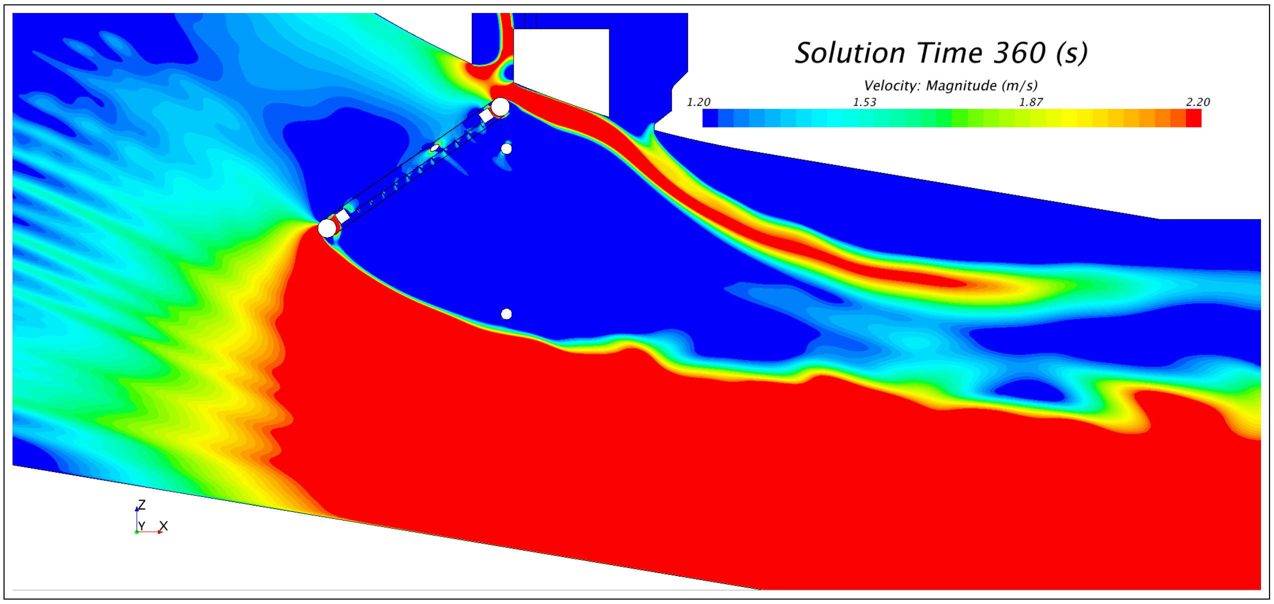
Solution Time 360 (s)
Velocity: Magnitude (m/s)
1.20
1.53
1.87
2.20

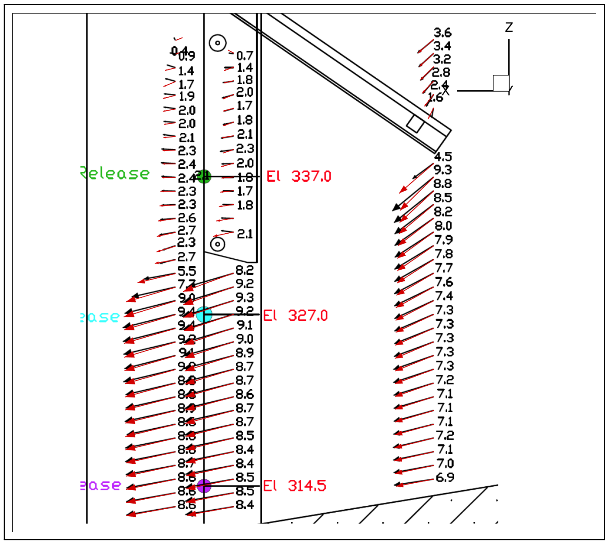
Release
El 337.0
El 327.0
El 314.5

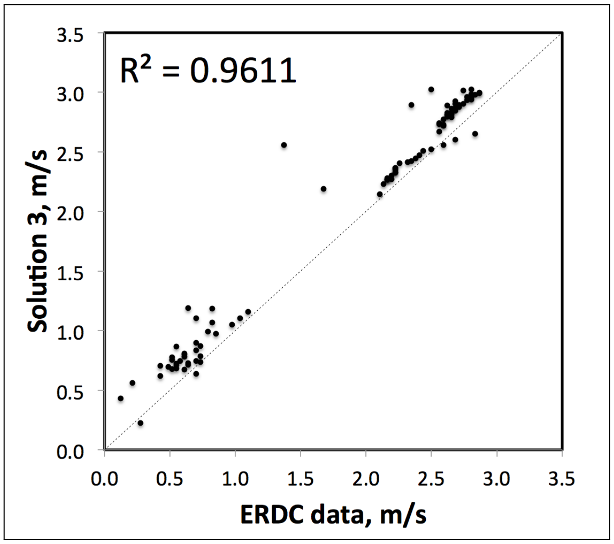
R^2 = 0.9611
Solution 3, m/s
ERDC data, m/s

SOLUTION 4

Dataset I

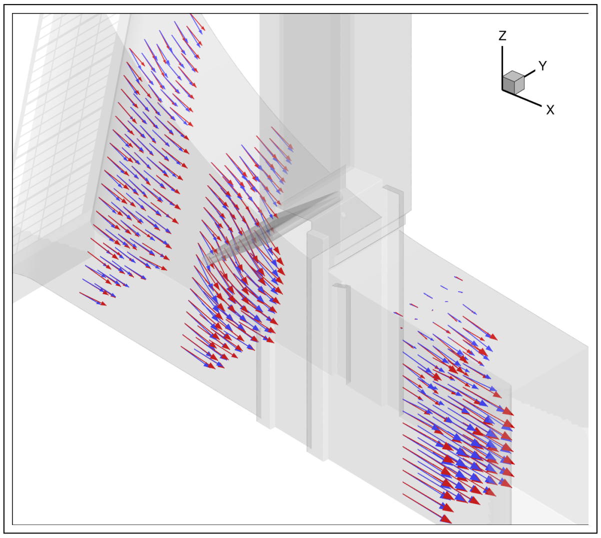

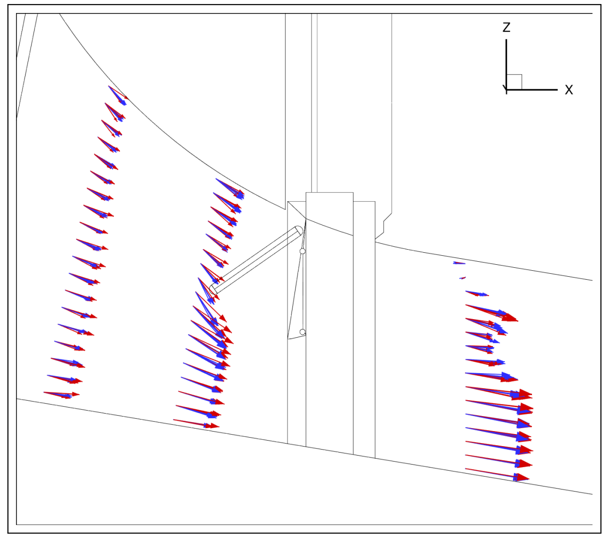

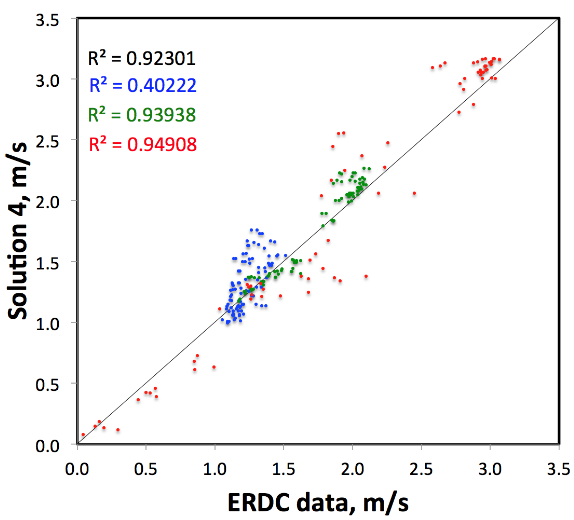

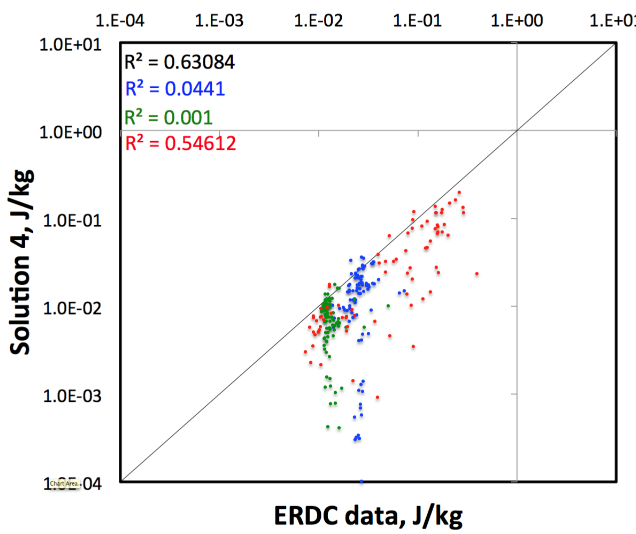

Dataset II

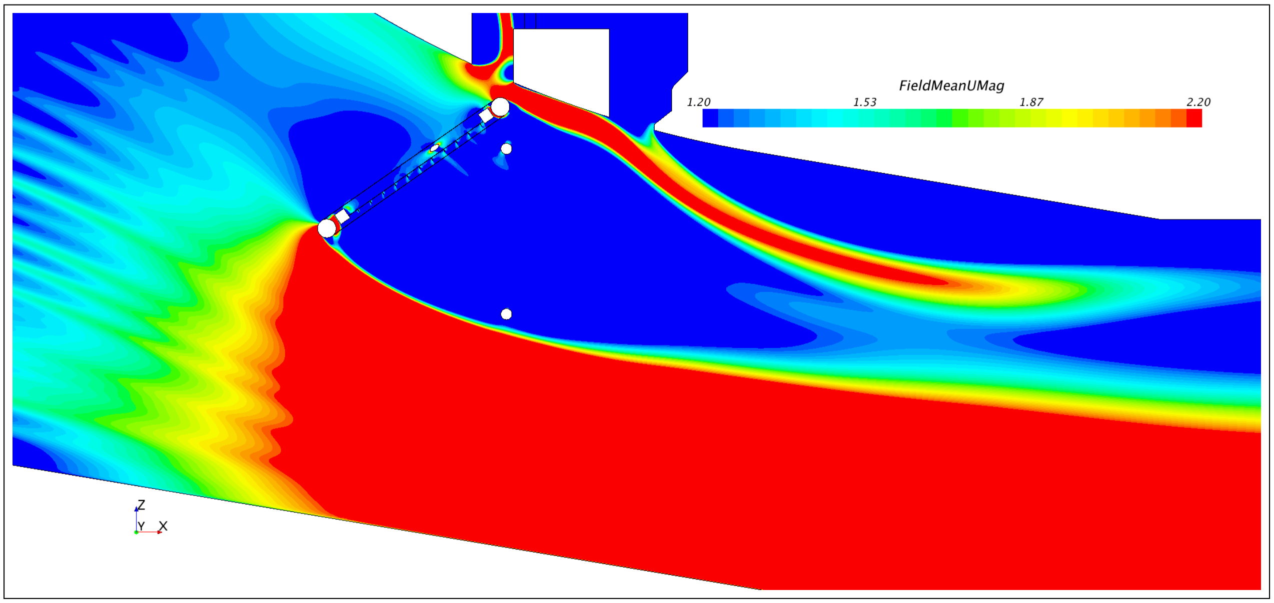
FieldMeanUMag
1.20
1.53
1.87
2.20
Z
Y
X

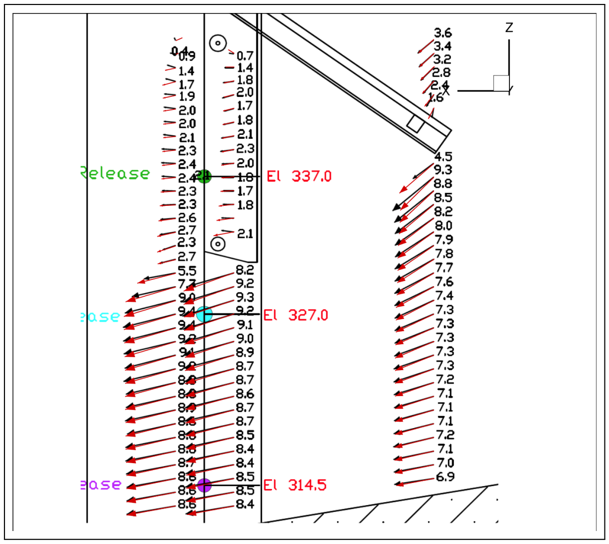
Release
El 337.0
El 327.0
El 314.5
Z

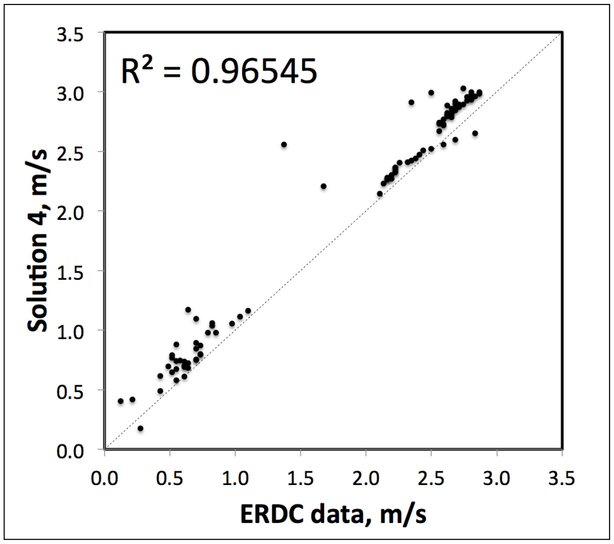
R^2 = 0.96545
Solution 4, m/s
ERDC data, m/s
0.0
0.5
1.0
1.5
2.0
2.5
3.0
3.5

SOLUTION 5

Dataset I

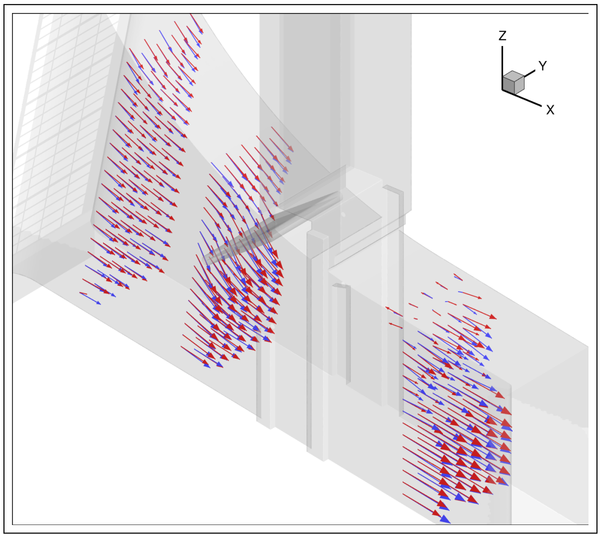

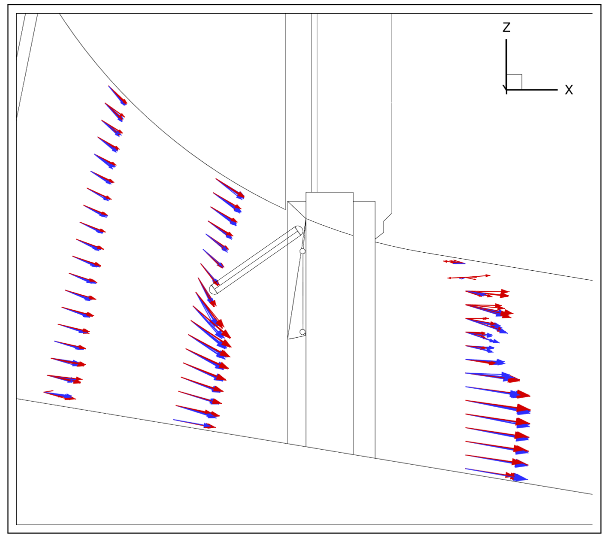

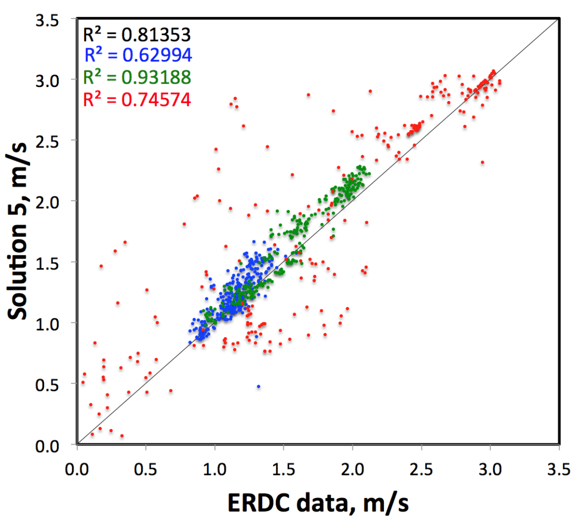

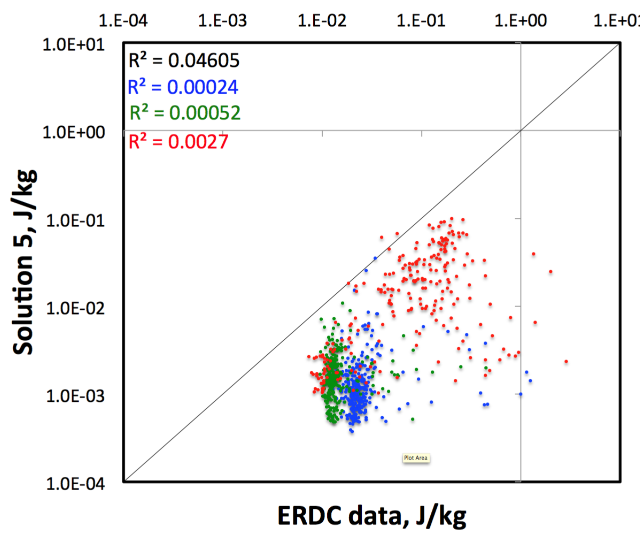

Dataset II

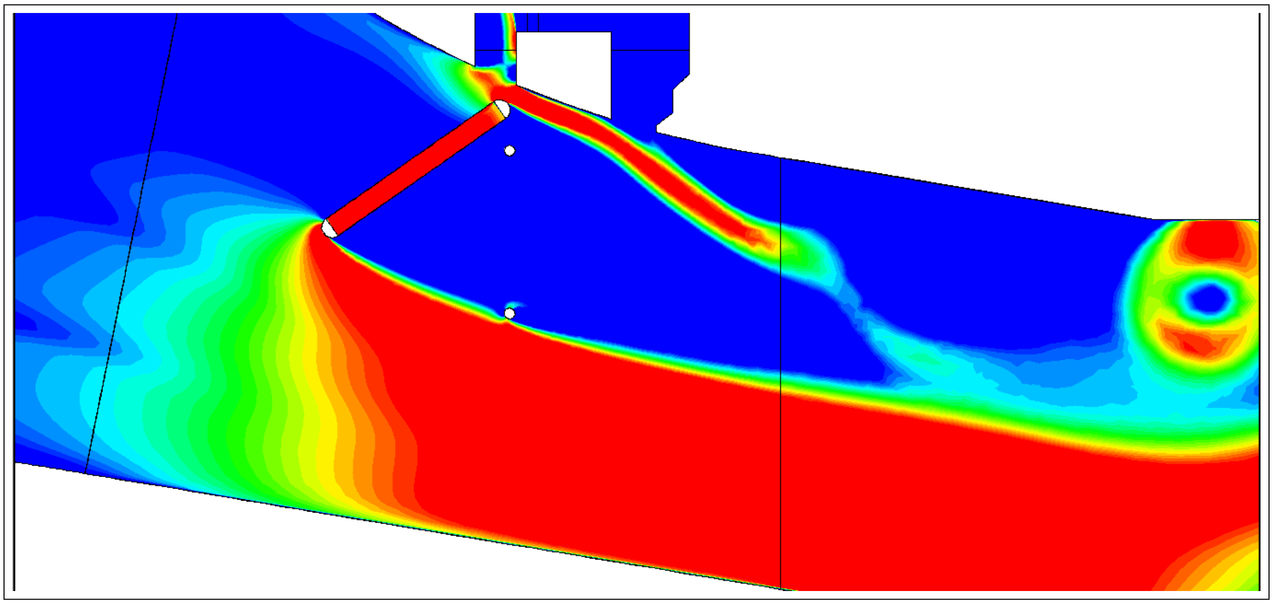

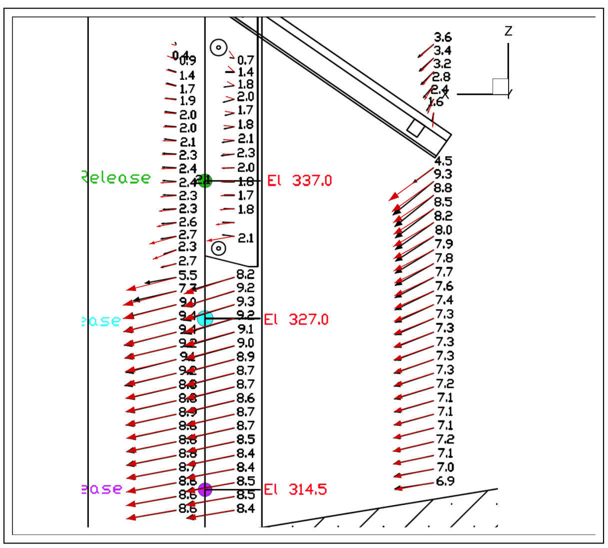
Release
El 337.0
El 327.0
El 314.5
Z

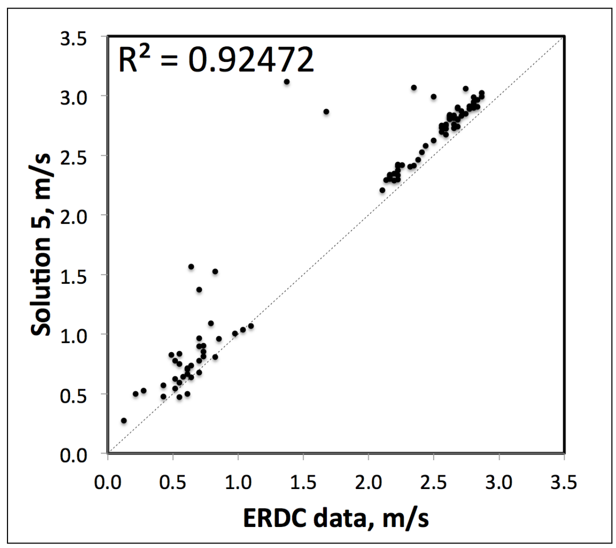
R^2 = 0.92472
Solution 5, m/s
ERDC data, m/s
0.0
0.5
1.0
1.5
2.0
2.5
3.0
3.5

SOLUTION 6

Dataset I

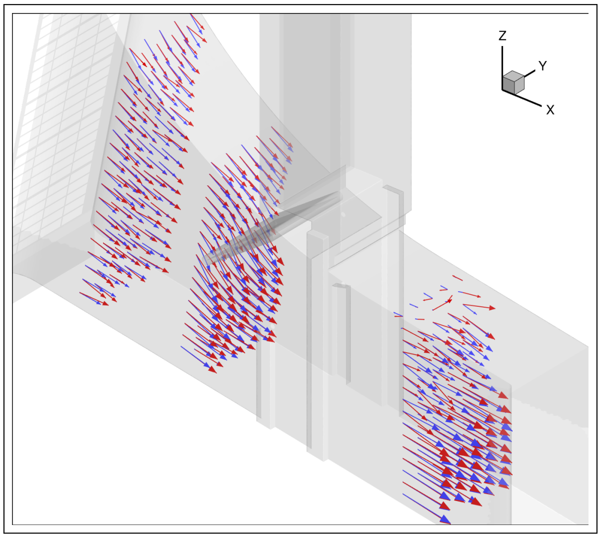

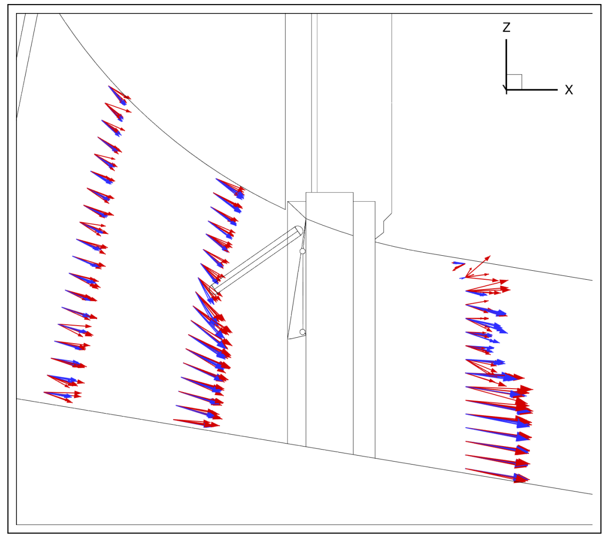

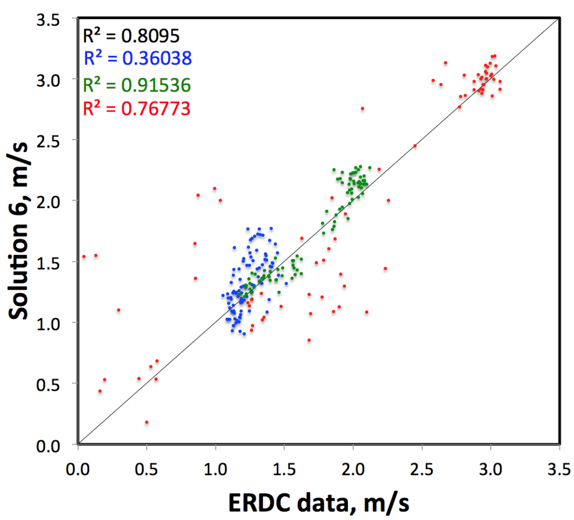

Dataset II

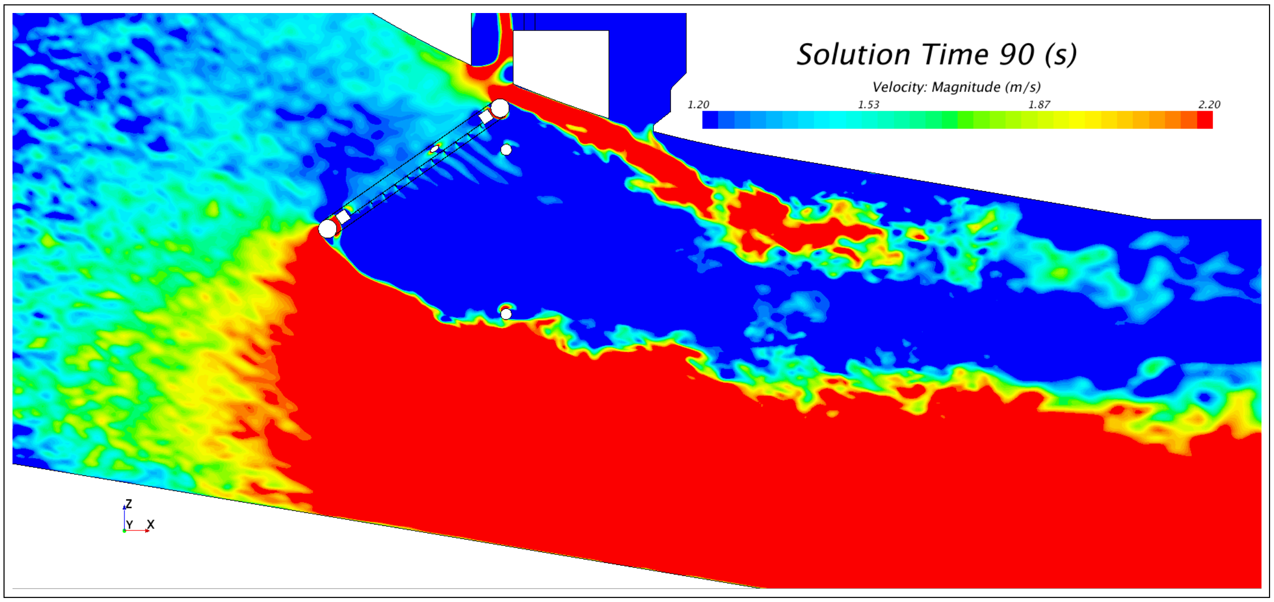
Solution Time 90 (s)
Velocity: Magnitude (m/s)
1.20
1.53
1.87
2.20

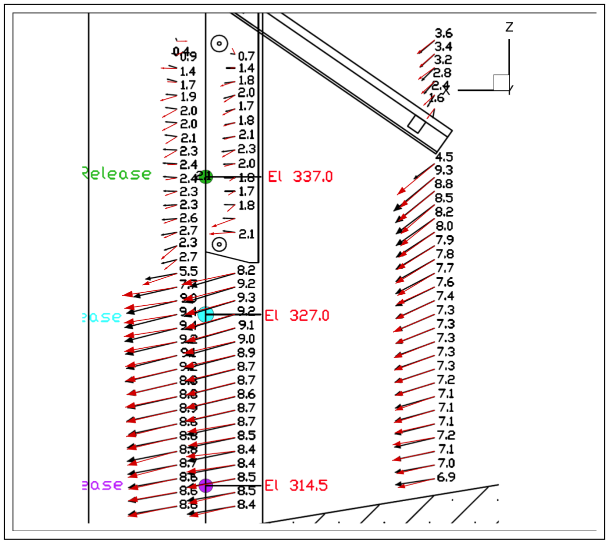

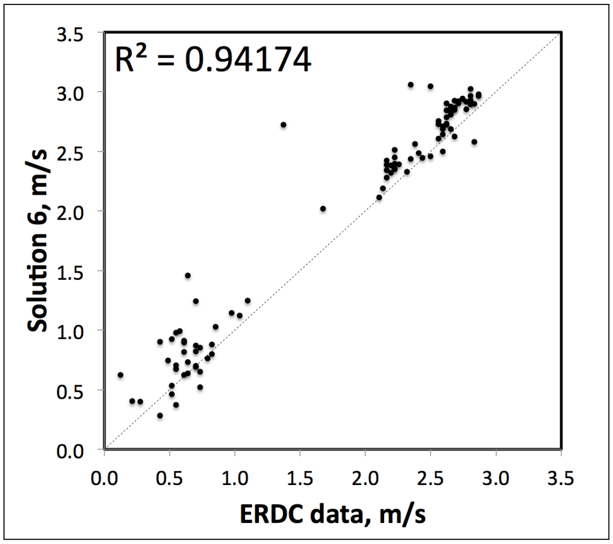
R^2 = 0.94174
Solution 6, m/s
ERDC data, m/s

Dataset I

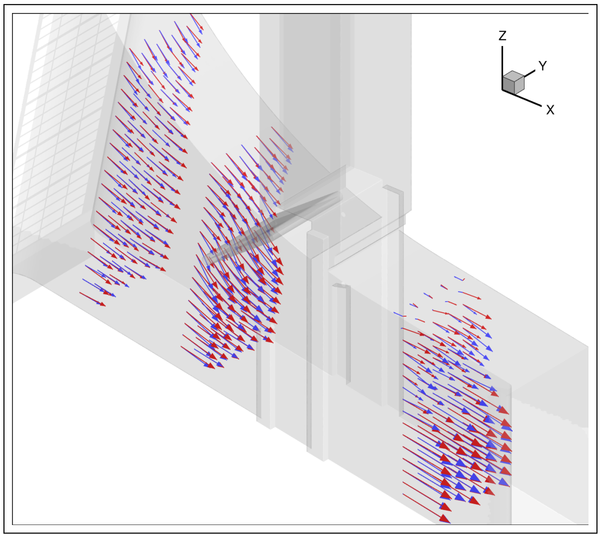

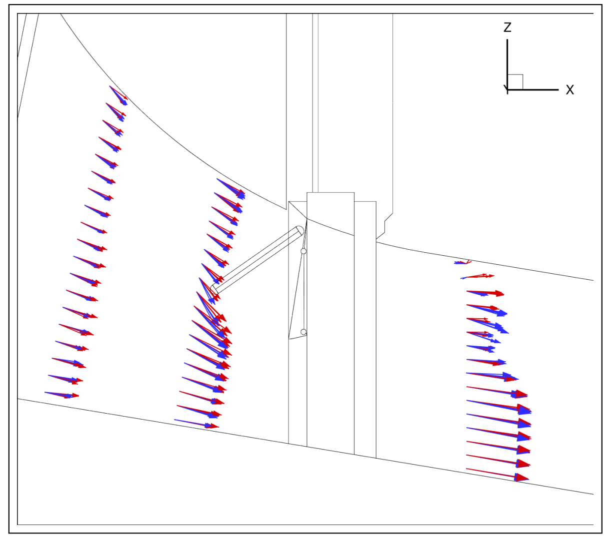
Z
X

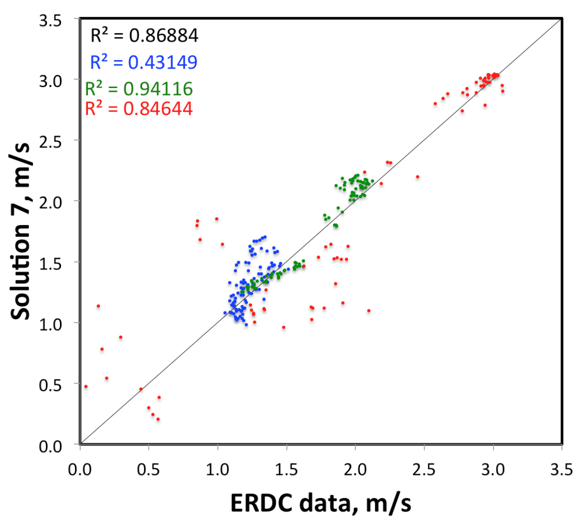
R^2 = 0.86884
R^2 = 0.43149
R^2 = 0.94116
R^2 = 0.84644
Solution 7, m/s
ERDC data, m/s
0.0
0.5
1.0
1.5
2.0
2.5
3.0
3.5

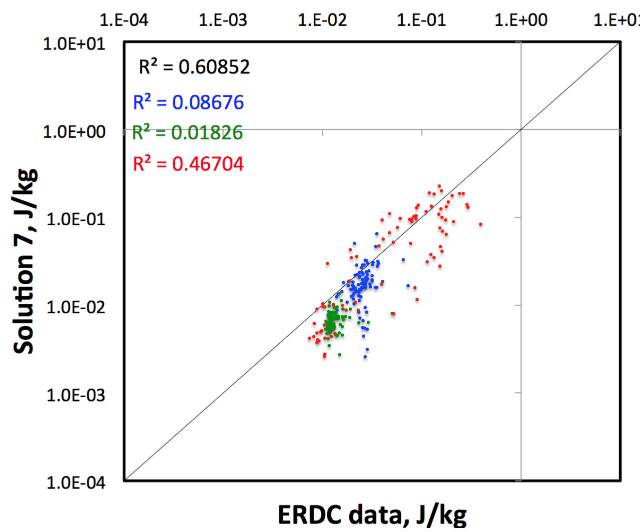
1.E-04
1.E-03
1.E-02
1.E-01
1.E+00
1.E+01
1.0E+01
1.0E+00
1.0E-01
1.0E-02
1.0E-03
1.0E-04
R^2 = 0.60852
R^2 = 0.08676
R^2 = 0.01826
R^2 = 0.46704
Solution 7, J/kg
ERDC data, J/kg

Dataset II

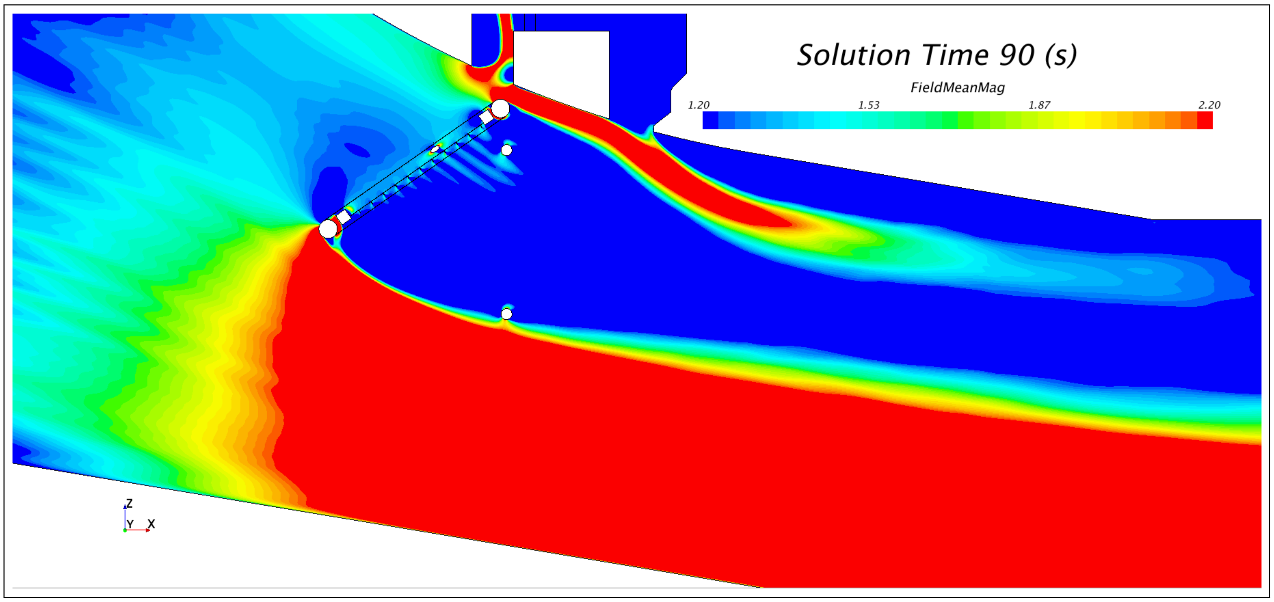
Solution Time 90 (s)
FieldMeanMag
1.20
1.53
1.87
2.20

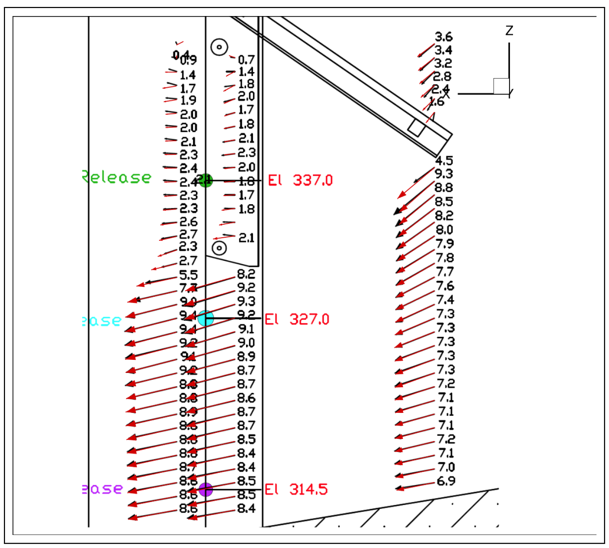
El 337.0
El 327.0
El 314.5

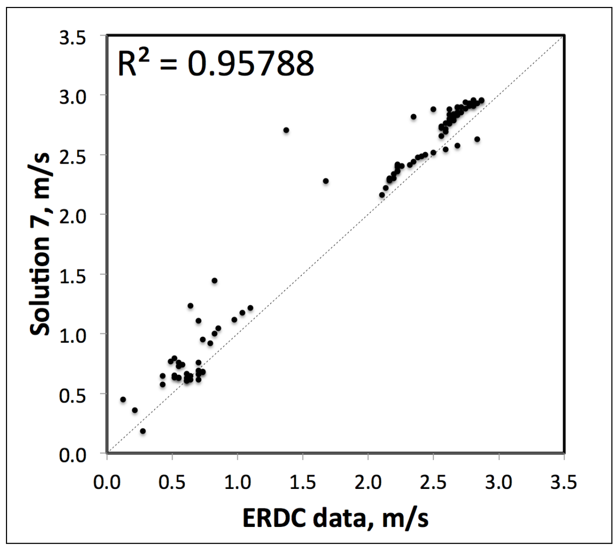
R^2 = 0.95788
Solution 7, m/s
ERDC data, m/s

SOLUTION 8

Dataset I

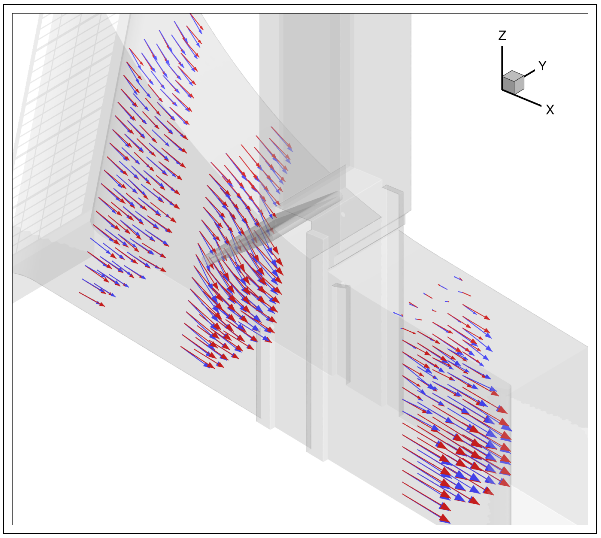

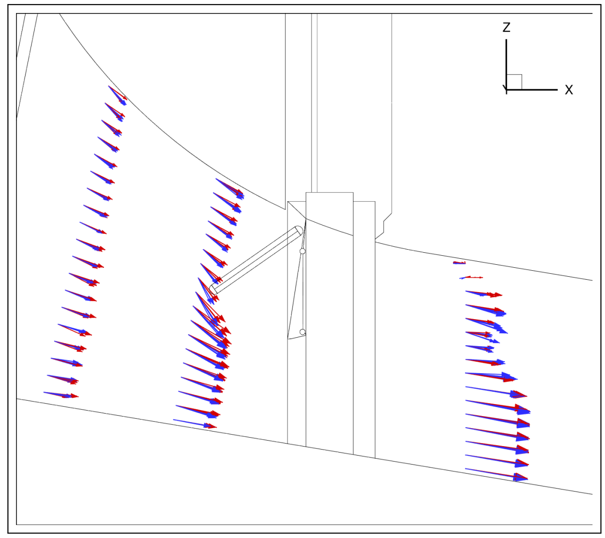

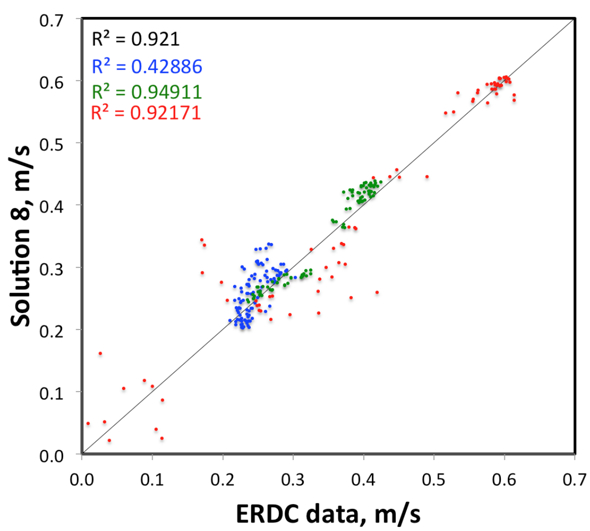

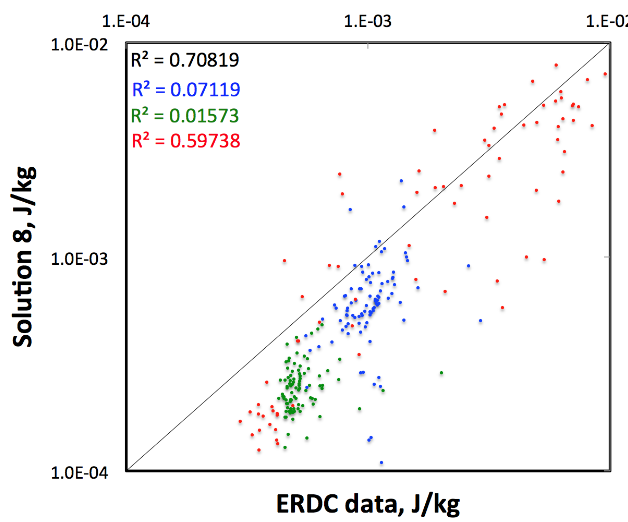

Dataset II

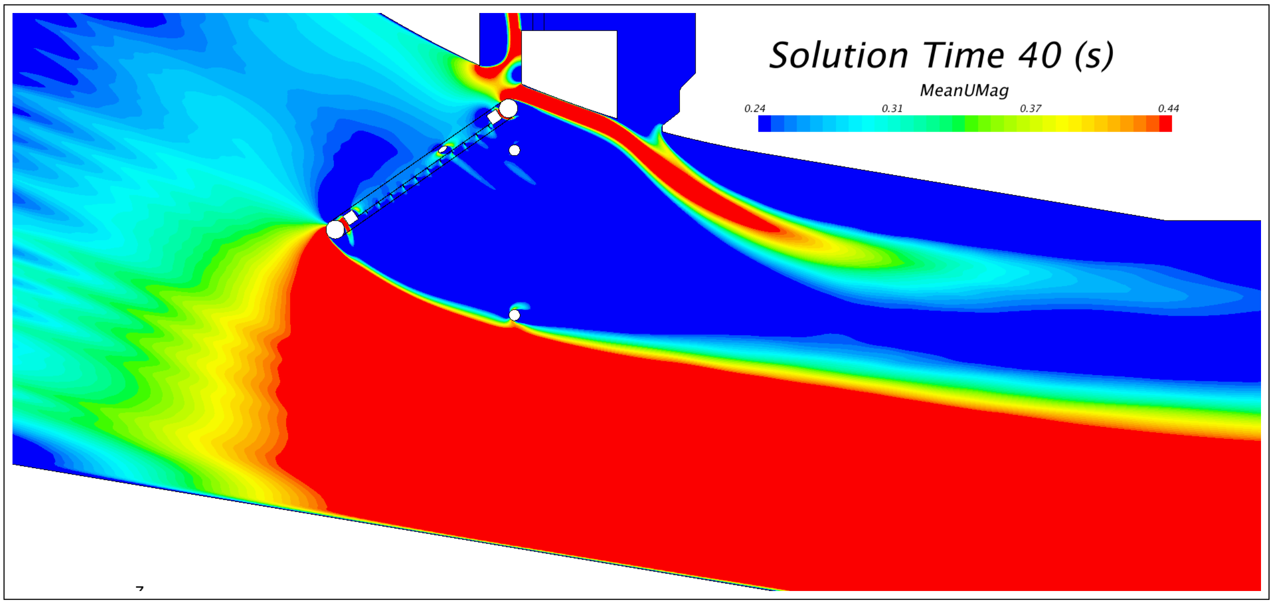

Solution Time 40 (s)
MeanUMag
0.24
0.31
0.37
0.44

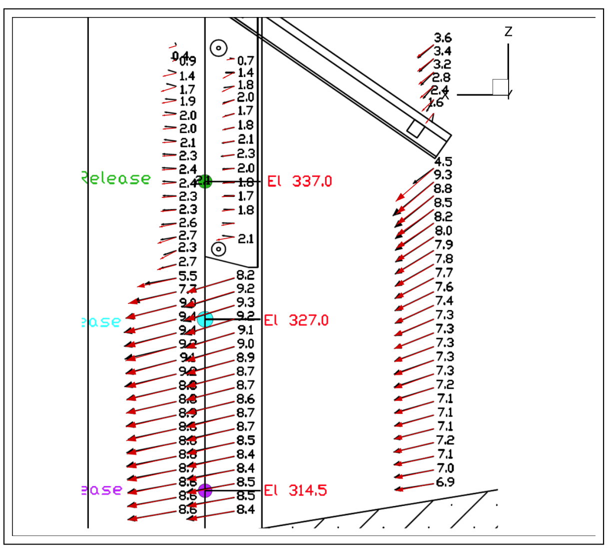

El 337.0
El 327.0
El 314.5

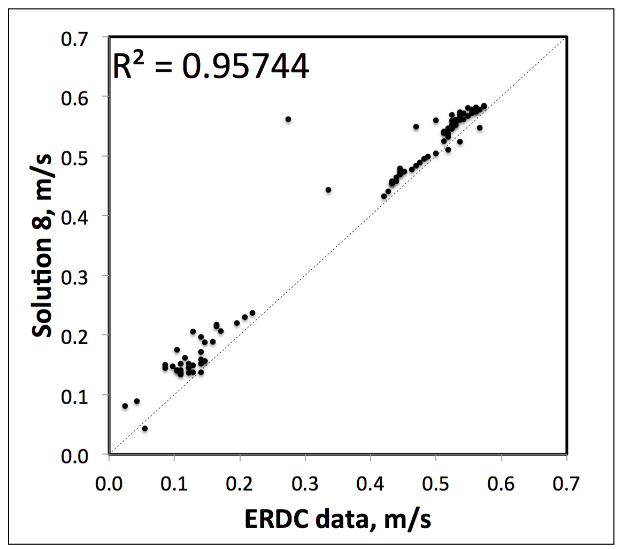

R^2 = 0.95744
Solution 8, m/s
ERDC data, m/s
0.0
0.1
0.2
0.3
0.4
0.5
0.6
0.7

SOLUTION 9

Dataset I

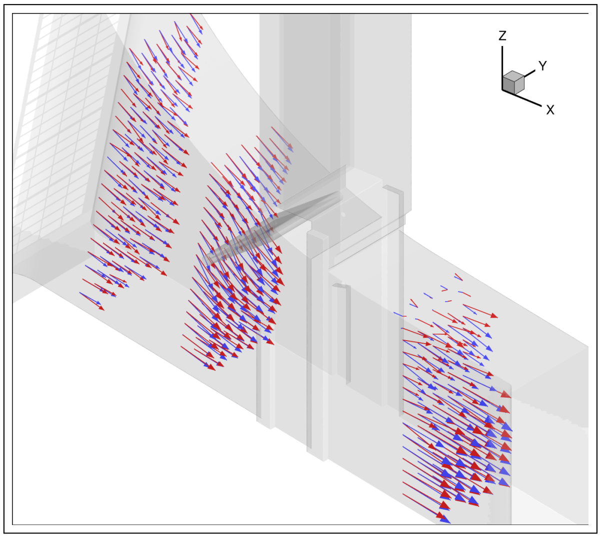

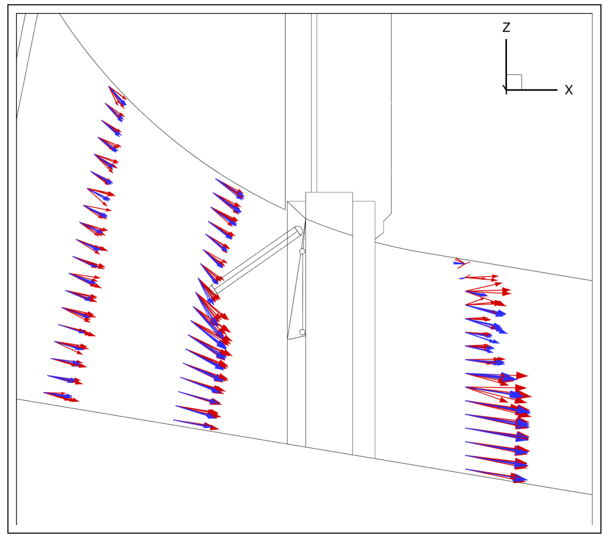

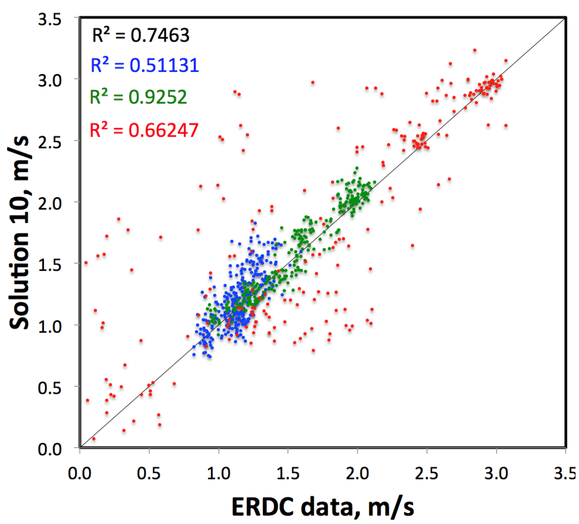

Dataset II

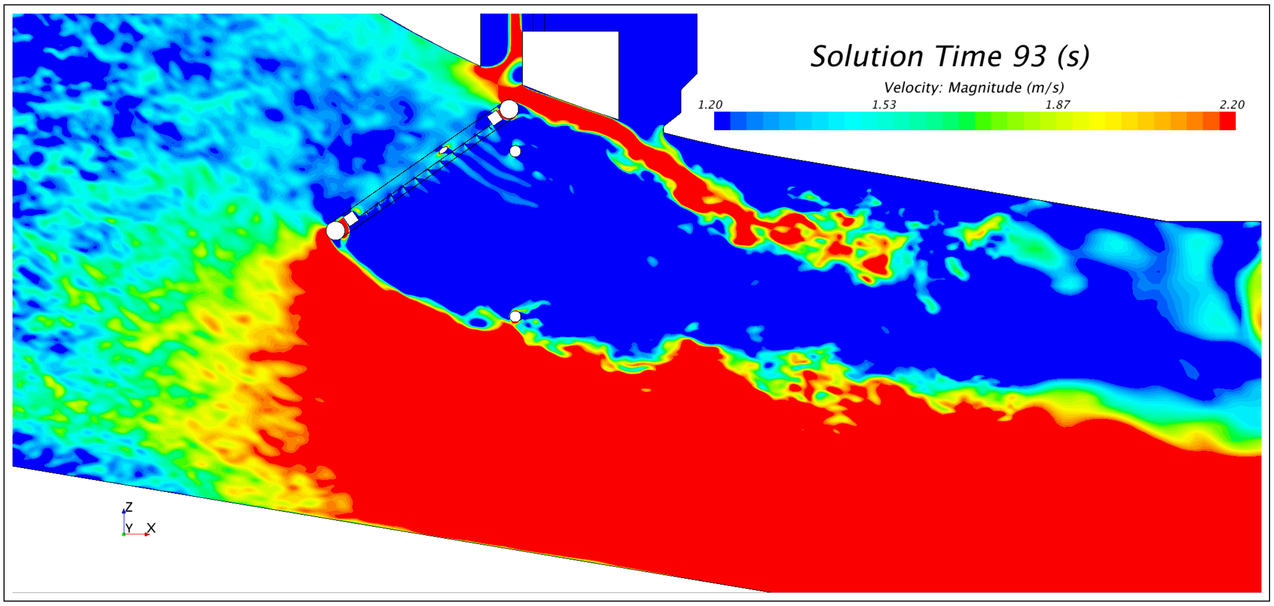
Solution Time 93 (s)
Velocity: Magnitude (m/s)
1.20
1.53
1.87
2.20
Z
Y
X

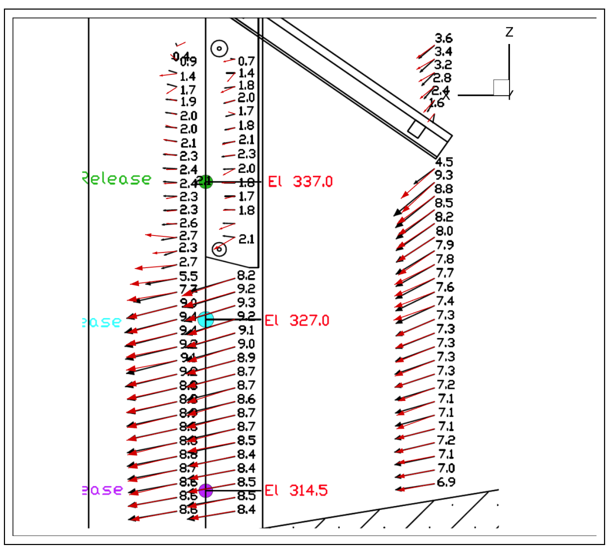
Release
El 337.0
El 327.0
El 314.5
Z

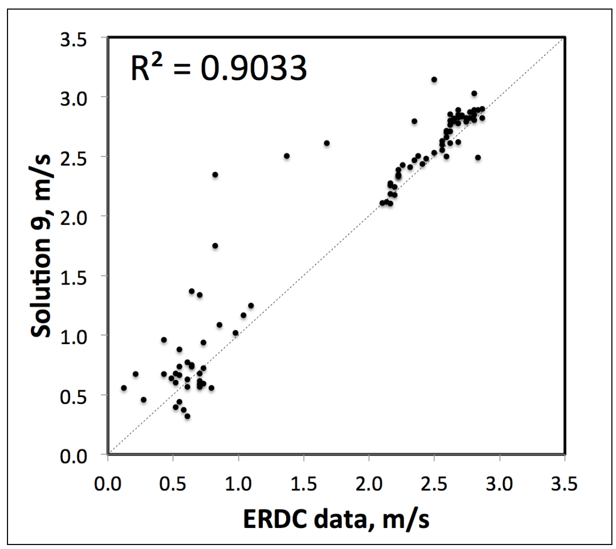
$R^2 = 0.9033$
Solution 9, m/s
ERDC data, m/s
0.0
0.5
1.0
1.5
2.0
2.5
3.0
3.5

SOLUTION 10

Dataset I

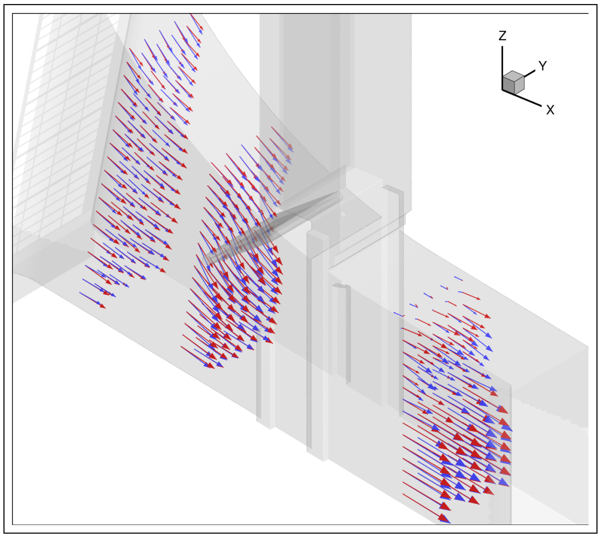

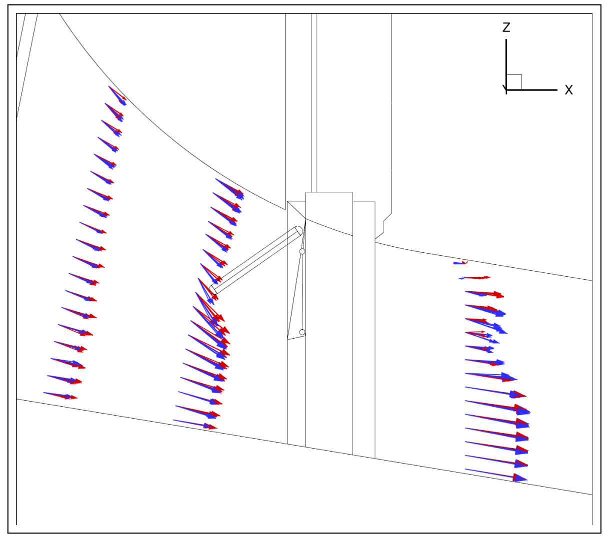

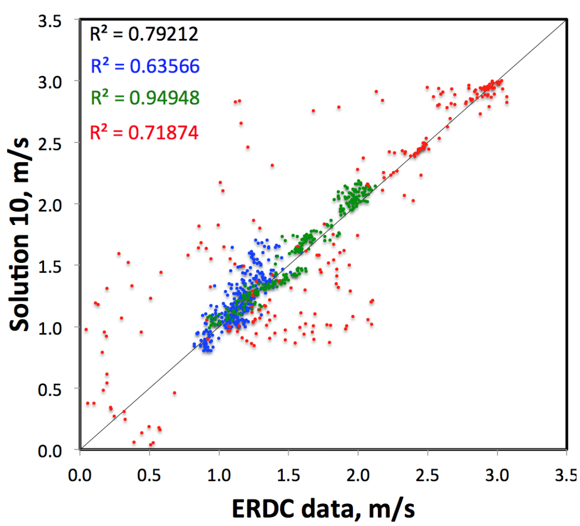

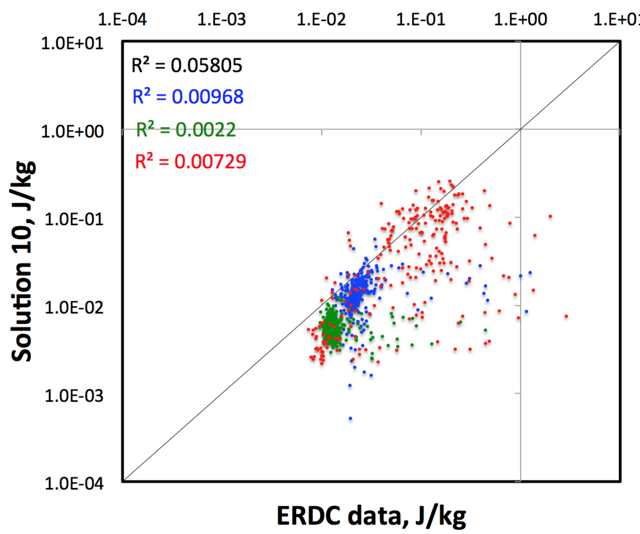

Dataset II

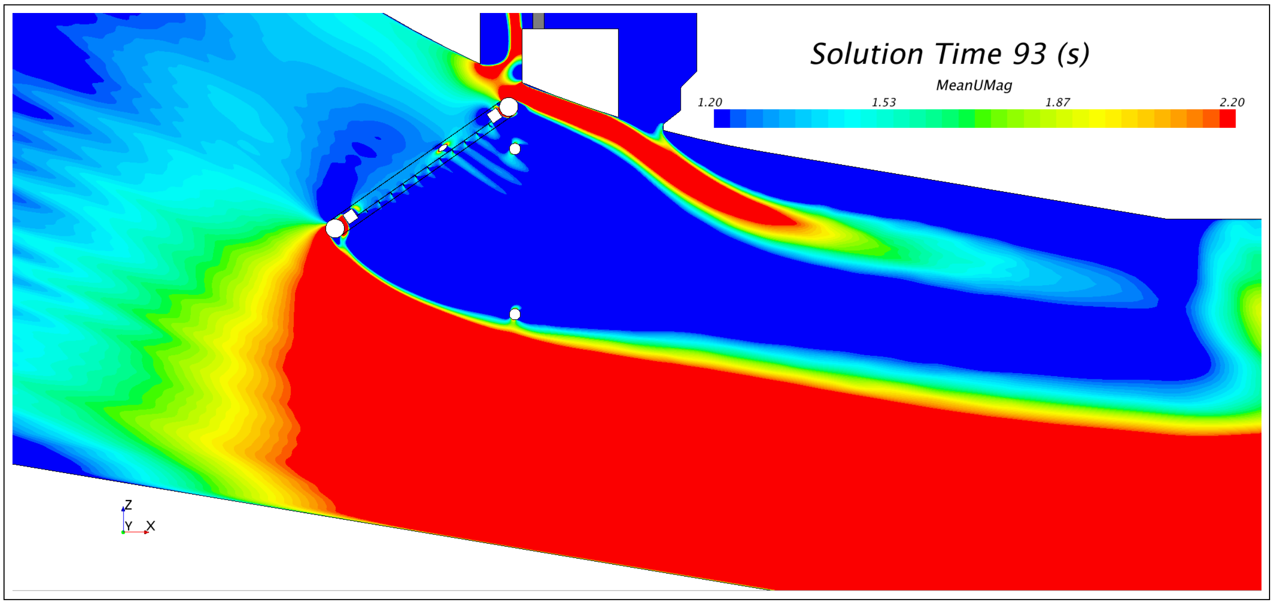

Solution Time 93 (s)
MeanUMag
1.20
1.53
1.87
2.20

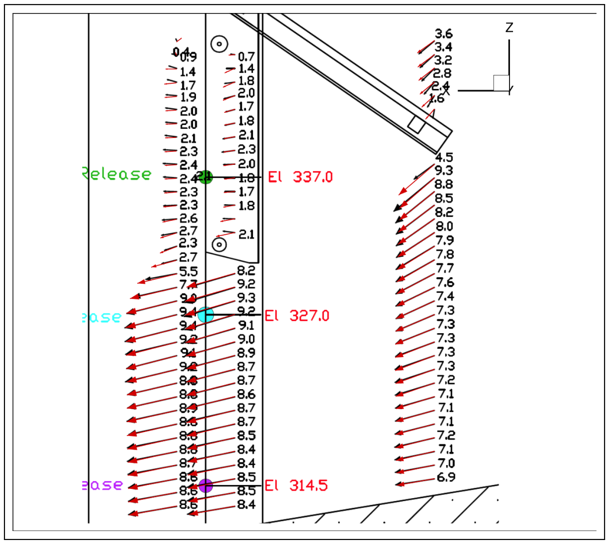

Release
El 337.0
El 327.0
El 314.5

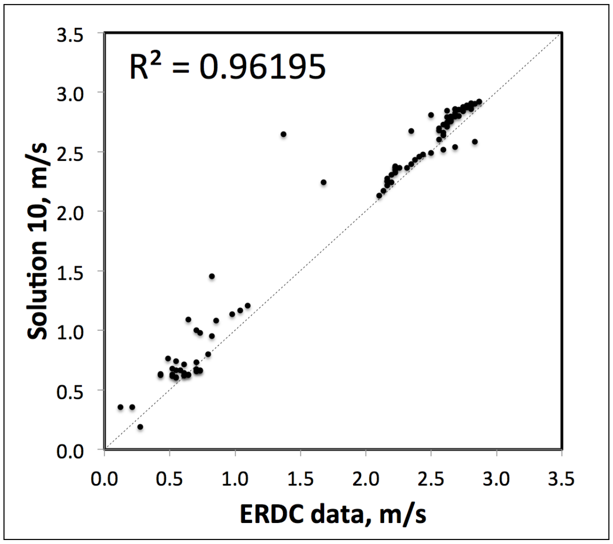

$R^2 = 0.96195$
Solution 10, m/s
ERDC data, m/s

Pacific Northwest
NATIONAL LABORATORY

U.S. DEPARTMENT OF
ENERGY

902 Battelle Boulevard
P.O. Box 999
Richland, WA 99352
1-888-375-PNNL (7665)
www.pnl.gov